Impact of MPEX Upsonde Observations on Ensemble Analyses and Forecasts of the 31 May 2013 Convective Event over Oklahoma

STACEY M. HITCHCOCK[a]

School of Meteorology, and Cooperative Institute for Mesoscale Meteorological Studies, University of Oklahoma, and NOAA/OAR/National Severe Storms Laboratory, Norman, Oklahoma

MICHAEL C. CONIGLIO

NOAA/OAR/National Severe Storms Laboratory, Norman, Oklahoma

KENT H. KNOPFMEIER

School of Meteorology, and Cooperative Institute for Mesoscale Meteorological Studies, University of Oklahoma, and NOAA/OAR/National Severe Storms Laboratory, Norman, Oklahoma

(Manuscript received 30 September 2015, in final form 10 May 2016)

ABSTRACT

This study examines the impact of assimilating three radiosonde profiles obtained from ground-based mobile systems during the Mesoscale Predictability Experiment (MPEX) on analyses and convection-permitting model forecasts of the 31 May 2013 convective event over Oklahoma. These radiosonde profiles (in addition to standard observations) are assimilated into a 36-member mesoscale ensemble using an ensemble Kalman filter (EnKF) before embedding a convection-permitting (3 km) grid and running a full ensemble of 9-h forecasts. This set of 3-km forecasts is compared to a control run that does not assimilate the MPEX soundings. The analysis of low- to midlevel moisture is impacted the most by the assimilation, but coherent mesoscale differences in temperature and wind are also seen, primarily downstream of the location of the soundings. The ensemble of forecasts of convection on the 3-km grid are improved the most in the first three hours of the forecast in a region where the analyzed position of low-level frontal convergence and midlevel moisture was improved on the mesoscale grid. Later forecasts of the upscale growth of intense convection over central Oklahoma are improved somewhat, but larger ensemble spread lowers confidence in the significance of the improvements. Changes in the horizontal localization radius from the standard value applied to the MPEX sounding assimilation alters the specific times that the forecasts are improved in the first three hours of the forecasts, while changes to the vertical localization radius and specified temperature and wind observation error result in little to no improvements in the forecasts.

1. Introduction

Convection-permitting numerical weather prediction (NWP) models have proven to be useful to forecasters tasked with alerting the public of the threat for severe weather (e.g., Kain et al. 2006; Clark et al. 2012). Part of the challenge of predicting convective weather in the short-term (0–9 h) using NWP models is the accurate analysis of ongoing storms in the initial conditions, for which the assimilation of radar data is essential (e.g., Dawson et al. 2012; Stratman et al. 2013; Yussouf et al. 2015). However, the characteristics of convective storms are strongly tied to the meso- and synoptic-scale environment in which they develop.

Stensrud and Gao (2010) examined the horizontal environmental variability in short-term forecasts and found that ensemble forecasts with horizontally inhomogeneous backgrounds performed better than those with homogeneous backgrounds, suggesting the importance of knowledge of horizontal environmental variability. Drylines,

[a] Current affiliation: Department of Atmospheric Science, Colorado State University, Fort Collins, Colorado.

Corresponding author address: Stacey M. Hitchcock, Department of Atmospheric Science, Colorado State University, 3915 W. Laport Ave., Fort Collins, CO 80523.
E-mail: smhitch@rams.colostate.edu

DOI: 10.1175/MWR-D-15-0344.1

© 2016 American Meteorological Society

Brought to you by NOAA Central Library | Unauthenticated | Downloaded 09/22/21 06:55 PM UTC

cold pools (gust fronts), and other boundaries can act as forcing mechanisms in convective initiation and storm organization (Hane et al. 1993; Weaver and Nelson 1982; Jewett and Wilhelmson 2006), so accurately representing the location, timing, and intensity of these features is necessary in order to improve forecasts of subsequent convection. For example, Sobash and Stensrud (2015) found that assimilation of surface mesonet data improved ensemble predictions of dryline location and the timing and placement of subsequent convective development. However, in order to consistently resolve important mesoscale features explicitly, NWP models and observational networks likely need even higher spatial and temporal resolution than what is currently available operationally (Sobash and Stensrud 2015). Therefore, it is important to continue to explore ways to improve the depiction of the mesoscale environment in model initial conditions, even for short-term forecasts (Stensrud et al. 2009; Benjamin et al. 2010; Wandishin et al. 2010; Romine et al. 2013).

a. *Data assimilation for convective-permitting forecasts*

Data assimilation is a process that combines observations and forecasts in an attempt to give the best estimate of the state of a physical system (Talagrand 1997; Kalnay 2003). The ensemble Kalman filter (EnKF; Evensen 1994) is a popular choice for the assimilation of observations on convection-permitting (1–4 km) model grids because of its ease of use relative to variational methods at these scales, and because it provides an efficient means of deriving flow-dependent relationships among model variables that are needed for effective data assimilation. Numerous studies have used EnKF methods to produce positive impacts on convective forecasts by assimilating radar data (Snyder and Zhang 2003; Dowell et al. 2004; Aksoy et al. 2009; Dawson et al. 2012; Marquis et al. 2014), surface data (Fujita et al. 2007; Wheatley et al. 2012; Knopfmeier and Stensrud 2013), satellite data (Jones et al. 2013, 2015), and various combinations of these data (Zhang et al. 2006; Snook et al. 2011; Romine et al. 2013; Yussouf et al. 2015).

While many of the studies above assimilate radiosonde profiles, they typically use soundings from the national radiosonde network, which is designed to sample the synoptic-scale environment. Although there are only three nonstandard soundings assimilated in this study, they effectively sample spatial and temporal scales smaller than what is sampled by the national radiosonde network. It is not clear if more closely spaced soundings should be assimilated in the same manner as the radiosonde profiles from the national network, and it is not clear if any particular variable or level sampled by the special radiosonde profiles might have more impact on the analysis than others.

Fabry and Sun (2010) and Fabry (2010) examined the potential impacts of various types of observations on convection-permitting forecasts and conclude that midlevel relative humidity (RH) measurements (and the reduction of RH initial condition errors) were shown to contribute the most to 0–6-h precipitation forecast skill on 4-km grids. They suggested that assimilation of RH measurements from radiosondes and/or integrated water vapor from microwave radiometers would be best to minimize RH errors (Fabry 2010). It was also suggested that measurements of low-level humidity, low- to midlevel temperature, and midlevel winds can have a positive impact on the skill of short-term precipitation forecasts. While methods to retrieve these variables from satellite and ground-based remotely sensed observations are improving (Bedka et al. 2009; Li et al. 2012; Wulfmeyer et al. 2015), the accuracy and vertical resolution of the retrieved profiles are still inferior to what can be obtained from radiosondes.

b. *Overview of the 31 May 2013 convection in Oklahoma*

During the evening of 31 May 2013, thunderstorms produced severe weather over much of Oklahoma (Fig. 1), including a large and strong tornado near El Reno, Oklahoma, that killed eight people and injured several others (Wurman et al. 2014). Additional storms formed on this storm's southwest flank and produced severe hail and winds in central Oklahoma in midevening (Figs. 1–3). A few hours later, an outflow boundary from the earlier storms helped support back-building convection (Figs. 3 and 4) that produced 6–7 in. (150–180 mm) of rain over much of the Oklahoma City, Oklahoma, metropolitan area and the deadliest flash flood in the state since 1984. Severe storms also extended from central Oklahoma to northeastern Oklahoma producing all forms of severe weather (large hail, high winds, and tornadoes; Fig. 1).

The mesoscale environment on 31 May 2013 was sampled by several balloon-borne radiosonde (upsonde) observations from ground-based mobile facilities as part of the Mesoscale Predictability Experiment [MPEX; see Trapp et al. (2016) and Weisman et al. (2015) for details]. The work discussed here addresses one of the objectives of MPEX to explore the impacts of assimilating afternoon preconvective upsonde observations on the analysis of the mesoscale environment, and examine those impacts on subsequent 0–9-h convection-permitting forecasts.

The primary goals of this paper are to outline a method of assimilating special radiosonde profiles into an experimental ensemble data assimilation and forecast system being developed at the National Severe Storms Laboratory (NSSL) and to examine the impacts of the assimilation on convection-permitting forecasts of

Brought to you by NOAA Central Library | Unauthenticated | Downloaded 09/22/21 06:55 PM UTC

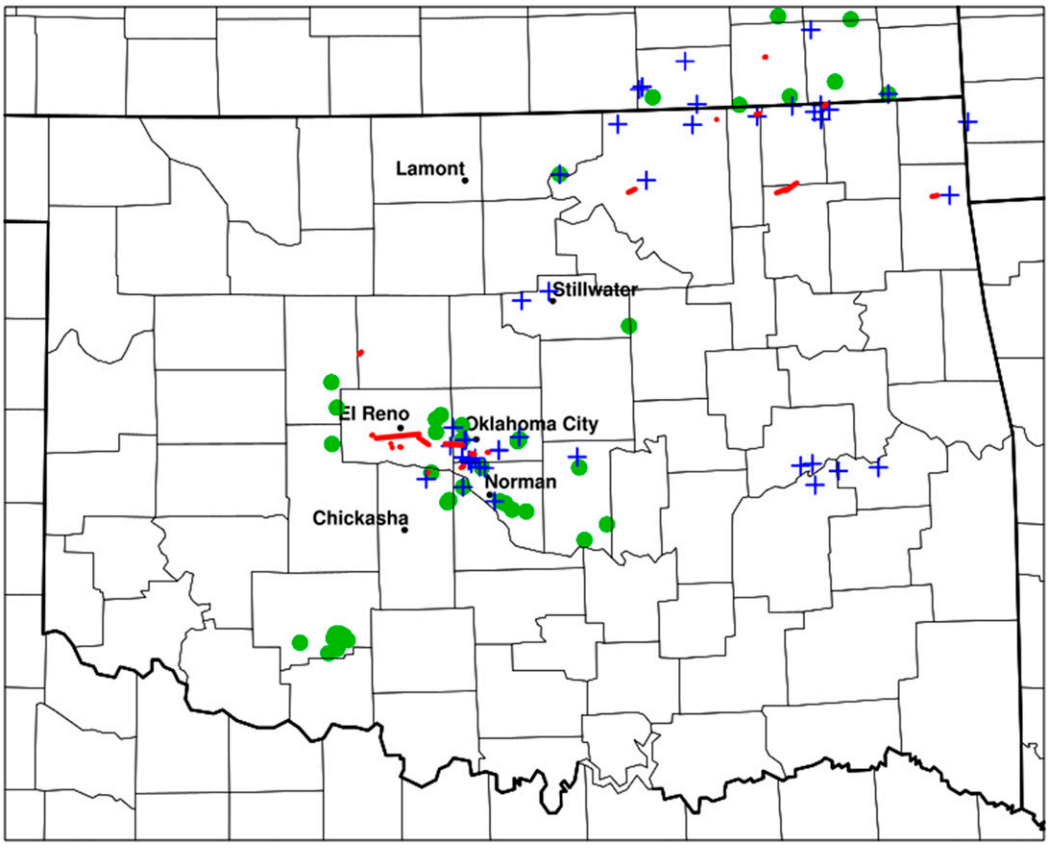

FIG. 1. Reports of tornadoes (red), wind gusts greater than 50 kt (blue; 1 kt = 0.5144 m s^{-1}), and hail equal to or greater than 1 in. (green), from the period 2000 UTC 31 May to 0500 UTC 1 Jun 2013 over Oklahoma received by the National Weather Service.

the 31 May 2013 convective event over Oklahoma. Tests of assimilation of multiple mobile soundings in a mesoscale model for convective forecast applications have not yet been reported in the literature. Although many interesting storm-scale phenomena occurred during this event (e.g., Wurman et al. 2014), the focus of this study is on the meso-β-scale (20–200 km) evolution. The ensemble data assimilation and modeling system, experimental design, and methods of evaluating the forecasts are described in section 2. Section 3 presents a comparison of the ensemble analyses and forecasts between the control run, a run that assimilates the MPEX soundings, as well as runs that test the sensitivity of the MPEX sounding assimilation to settings in the data assimilation. Section 4 presents a summary and discusses some implications of the results and future research directions.

2. Methods

The WRF Model ARW-core version 3.4.1 configured with the Data Assimilation Research Testbed (DART) Lanai version (Anderson and Collins 2007; Anderson et al. 2009) is used for data assimilation and ensemble forecasting. The domain used for data assimilation has 235 × 340 grid points spaced 15 km apart and covers the contiguous United States (CONUS) with 51 vertical levels and a model top of 50 hPa (Fig. 5). A 36-member ensemble is created by downscaling the 0000 UTC 31 May 2013 Global Ensemble Forecast System (GEFS) 50-km analyses for initial conditions (ICs), and forecasts from this GEFS cycle are used as lateral boundary conditions (LBCs) for the 15-km grid. Since the 2013 version of the GEFS only had 20 members, a different IC could not be used for each of the 36 members of the WRF ensemble. Therefore, the first 18 members of the GEFS are used to create ICs for two sets of 18 ensemble members. This approach uses the first 18 members of the GEFS and makes the initial conditions for member n and member $36 + 1 - n$ equivalent (the ICs for member 1 were also used for member 36, member 2 for 35, etc.). The two members with the same ICs and LBCs use a different set of physics as shown in Table 1 so that no two members are configured the same.

Brought to you by NOAA Central Library | Unauthenticated | Downloaded 09/22/21 06:55 PM UTC

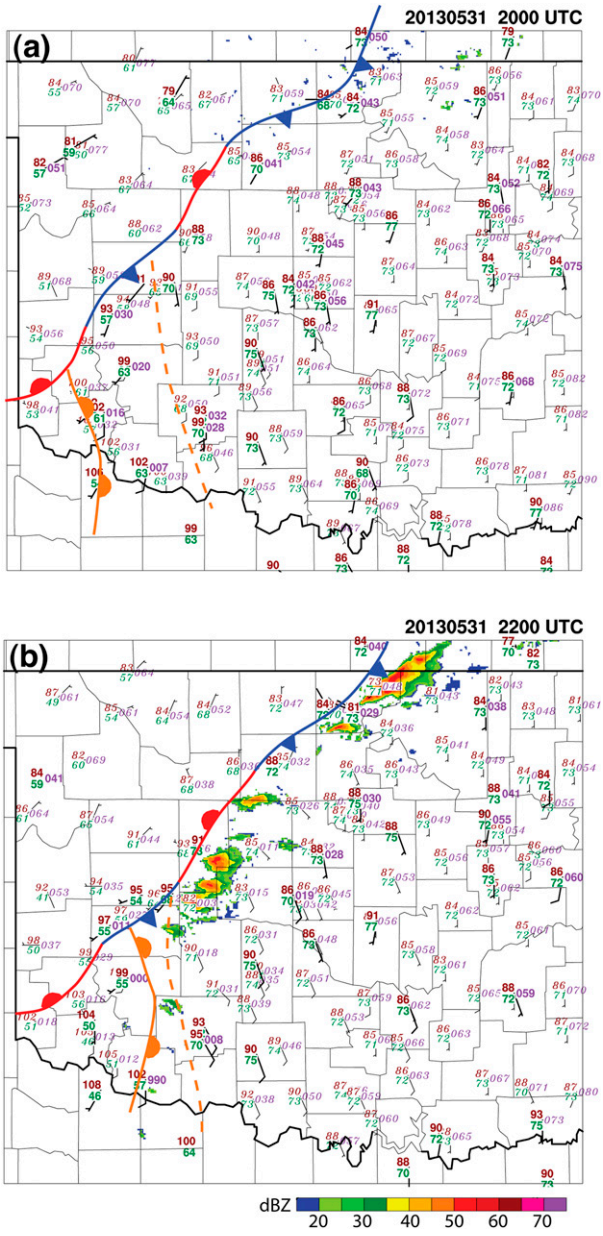

FIG. 2. METAR and Oklahoma Mesonet surface observations showing temperature (red) and dewpoint (green) in °F and pressure reduced to sea level (purple) in hPa (with the leading digit removed) valid at (a) 2000 and (b) 2200 UTC. Half (full) wind barbs depict 5 (10) kt. Oklahoma mesonet observations have italicized font. An analysis of composite (column maximum) reflectivity from the NSSL National Mosaic and MultiSensor Quantitative Precipitation Estimates system (Zhang et al. 2011) and manually drawn boundaries referred to in the text also are shown.

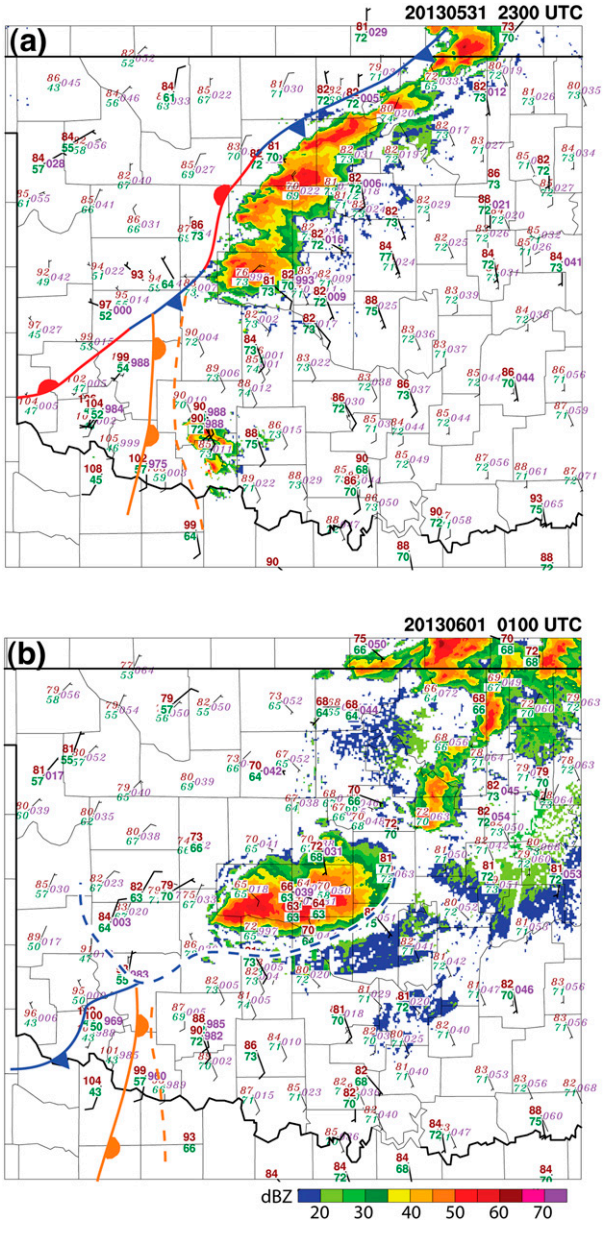

FIG. 3. As in Fig. 2, but for (a) 2300 UTC 31 May and (b) 0100 UTC 1 Jun.

a. Data assimilation

Observations were obtained from the Meteorological Assimilation Data Ingest System (MADIS; Miller et al. 2007) that include 1) mandatory and significant levels from the NWS radiosondes; 2) surface data from aviation routine weather reports (METARs), marine (ship and buoy) reports, the Oklahoma Mesonet, and the National Mesonet; 3) the Aircraft Meteorological Data Relay (AMDAR) reports for wind and temperature; and 4) atmospheric motion vectors (AMVs) derived from satellite observations. These observations are assimilated every hour from 0100 to 1600 UTC using the ensemble adjustment Kalman filter (EAKF; Anderson 2001) encoded within the DART software. The assimilation was performed half-hourly from 1600 to 2000 UTC

Brought to you by NOAA Central Library | Unauthenticated | Downloaded 09/22/21 06:55 PM UTC

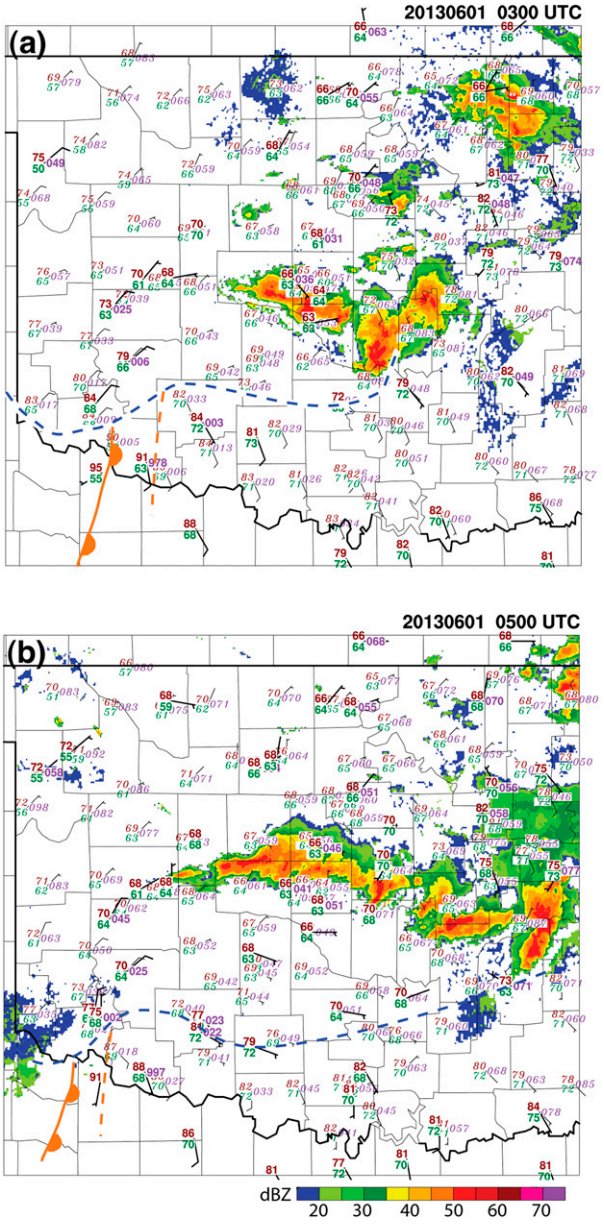

FIG. 4. As in Fig. 2, but for (a) 0300 and (b) 0500 UTC 1 Jun.

with observations binned into half-hour intervals centered at the top and bottom of the hour. All data were assimilated onto the full 15-km grid domain except for the National and Oklahoma mesonet observations, which were assimilated onto the 15-km grid only over the area covered by the 3-km grid (Fig. 5). Adaptive inflation (Anderson 2007) is applied to the ensemble of forecasts prior to the assimilation step to help maintain spread.

The 36-member ensemble of analyses valid at 2000 UTC are downscaled to create ICs for a convection-permitting (3 km) grid (Fig. 5). Forecasts run on the 15-km grid beginning at 2000 UTC serve as the LBCs for the 3-km grid. The initialization time was chosen to be 2000 UTC to allow for at least 1 h of integration time on the 3-km grid prior to convective initiation (CI) in the area of interest (Oklahoma). Model reflectivity in early output times was examined, as downscaling from 15 to 3 km can produce noisy convection early in a forecast. Convection that initiated after 60 min appeared realistic in reflectivity, maintained relatively strong updrafts, and produced cold pools comparable to those in later forecast times, and is therefore included in the evaluation. Convective initiation first occurred shortly after 2100 UTC along the front in Oklahoma, then between 2130 and 2150 UTC in west-central Oklahoma (Figs. 2a,b). The set of 36 forecasts are then run 9 h (to 0500 UTC 1 June) on the 3-km grid that use the same physics options as those for the parent grid (Table 1), except that no cumulus parameterization is used. The resulting analyses and forecasts compose the control run for this study. The goal of this approach is to make the control run representative of the best possible forecast that could have been made given all of the observations that were available in the operational data stream at the time.

On 31 May 2013, three soundings were obtained prior to convective initiation (Fig. 6). One radiosonde was released at 1610 UTC in Norman, Oklahoma, by a team from NSSL (Fig. 6d). Another was released by a mobile unit from the State University of New York at Oswego[1] at 1801 UTC near Stillwater, Oklahoma (Fig. 6b), and the third was released at 1920 UTC near Chickasha, Oklahoma, by a team from Colorado State University (CSU) (Fig. 6c).

The MPEX soundings sample every 1–2 s during the balloon ascent, and therefore, the observations (and their errors) are likely correlated in time and space. The assimilation of densely spaced, highly correlated observations can be harmful to the analysis (Liu and Rabier 2002). To mitigate this, the MPEX sounding data are thinned by defining ''significant'' levels at which a substantive change in temperature, dewpoint, or wind occurs, similar to how the NWS radiosonde data are routinely thinned. This helps retain potentially meaningful meteorological features in the assimilation while mitigating the effects of correlated observation errors.

The data were binned into half-hour windows (for the CSU sounding, the observations taken between 1920 and 1944 UTC are valid at 1930 UTC and the observations taken between 1945 and 2014 UTC are valid at 2000 UTC). Finally, the true position of the sonde is

[1] The State University of New York at Oswego was not officially a part of MPEX.

Brought to you by NOAA Central Library | Unauthenticated | Downloaded 09/22/21 06:55 PM UTC

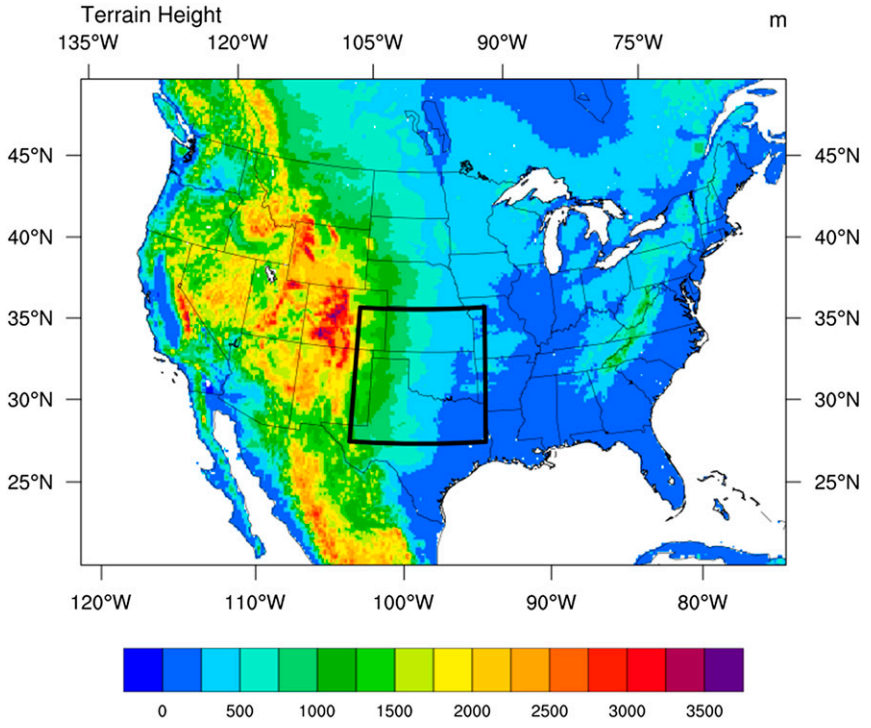

FIG. 5. The 15-km WRF-DART domain with terrain height (m) contoured. The 3-km domain is shown by the black box.

assimilated, effectively taking the balloon drift shown in Fig. 6a into account.[2]

It should be noted that two special NWS soundings were released in the area during the period when MPEX soundings are assimilated, one valid at 1800 UTC at Norman and one valid at 1700 UTC in Lamont, Oklahoma (Fig. 6a). A third special NWS sounding was released at 1800 UTC in Springfield, Missouri, just northeast of our nested domain. The control run refers to the run that includes these special NWS soundings. The experiment that assimilates both the special NWS soundings and the MPEX soundings is referred to as the MPEX run.

b. Sensitivity experiments

In the same manner as the control and MPEX runs, two additional experiments were performed to test the sensitivity of the impact of the MPEX soundings to the inclusion of the special NWS soundings. One run was performed that excluded both the MPEX soundings and special NWS soundings (hereafter NONWS). The second run included the MPEX soundings, but not the NWS soundings (hereafter MPEX_NONWS). In comparing these runs to the control and MPEX runs described, it is possible to see the individual impacts of the MPEX soundings and the special soundings compared to the combined impact of all six soundings assimilated in the 4 h before the start of the forecast.

Furthermore, the sensitivity of the mobile sounding assimilation to the horizontal and vertical localization is explored to examine if the special radiosonde profiles should be assimilated in the same manner as the radiosonde profiles from the national network. Localization reduces the impact of spurious correlations between an observation and model state variables far from the observation location that arise from small ensemble sizes. By weighting the impact of observations on the model state as a function of distance, sampling errors can be reduced. This study employs the common way to localize variables by multiplying the error covariance estimate in the EAKF with a Gaussian-like weighted correlation function (Gaspari and Cohn 1999) that decreases to 20% of its original weight at a "cutoff" radius. The MPEX soundings were released in close proximity to sample the subsynoptic-scale environment, so a localization radius smaller than that used for the NWS soundings, which are released at spatial and temporal frequencies designed sample the synoptic-scale environment, may be appropriate.

[2] Typical NWS sondes are assumed to profile the atmosphere directly above the launch site. Notably the drift measurement locations for soundings are available within standard bufr observation files (see Laroche and Sarrazin 2013).

Brought to you by NOAA Central Library | Unauthenticated | Downloaded 09/22/21 06:55 PM UTC

TABLE 1. Multiphysics for the first 18 members: ellipses in categories for members 7–12 and 13–18 indicate repetition of the PBL and radiation options.

Member	Microphysics	Cumulus	PBL	Land surface	Radiation	
					SW	LW
1	Thompson	Kain–Fritsch	YSU	RAP	Dudhia	RRTM
2	Thompson	Kain–Fritsch	YSU	RAP	RRTMG	RRTMG
3	Thompson	Kain–Fritsch	MYJ	RAP	Dudhia	RRTM
4	Thompson	Kain–Fritsch	MYJ	RAP	RRTMG	RRTMG
5	Thompson	Kain–Fritsch	MYNN	RAP	Dudhia	RRTM
6	Thompson	Kain–Fritsch	MYNN	RAP	RRTMG	RRTMG
7–12	Thompson	Grell	⋯	RAP	⋯	⋯
13–18	Thompson	Tiedtke	⋯	RAP	⋯	⋯

The horizontal and vertical cutoff radii used for the NWS soundings and for the MPEX soundings are approximately 230 and 4 km, respectively, the same as those used for a similar application in Wheatley et al. (2014). Sensitivity experiments with the MPEX soundings included doubling (460 km) and halving (115 km) the horizontal cutoff radius, halving the vertical cutoff radius (2 km), and making the vertical cutoff radius so large (20 km) that the covariances are altered little over the troposphere (Table 2). For the cases in which the horizontal cutoff radius was varied, the vertical cutoff radius was not changed and vice versa.

Additionally, the sensitivity to smaller specified temperature and wind observation errors (referred to as the ''lowobserr'' experiment) to those compared to the standard values are explored (Fig. 7). Consideration of observation errors is required in the use of the EAKF and reflects the combined effects of instrument error, representativeness error, and differences in the scale of measurable structures by the sensor and the smallest resolvable structures in the model. The default list of specified observation errors for all observation types follows those used in Romine et al. (2013, see their Table 3). The representativeness error for the MPEX soundings could be assumed to be lower than that for the NWS soundings because the NWS radiosondes are made to be valid at a single time whereas the MPEX soundings are binned into half-hour windows. Furthermore, the NWS radiosonde profiles are assumed to be valid at a fixed horizontal location—the ground location of the launch—whereas the exact position of the sonde in its flight is used to assimilate the MPEX observations.

c. Ensemble evaluation

Bias, root-mean-square error (RMSE), total error (or total spread), and the consistency ratio (CR) are used to evaluate the analyses on the 15-km grid and are given by

$$\text{bias} = \frac{1}{N_o}\sum_{n=1}^{N_o}\overline{H(\mathbf{x}_n^{f,a})} - y_n, \tag{1}$$

$$\text{RMSE} = \sqrt{\frac{\sum_{n=1}^{N_o}\left[\overline{H(\mathbf{x}_n^{f,a})} - y_n\right]^2}{N_o - 1}}, \quad \text{and} \tag{2}$$

$$\text{total spread} = \sqrt{\sigma_o^2 + \left\{\frac{1}{(N_e - 1)}\sum_{n=1}^{N_e}\left[H(\mathbf{x}_n^{f,a}) - \overline{H(\mathbf{x}^{f,a})}\right]^2\right\}}, \tag{3}$$

where H is the forward operator that maps the model prior analysis (forecast) $\mathbf{x}_n^f$, or posterior analysis $\mathbf{x}_n^a$, to the observation location and type y_n; N_o is the number of observations; N_e is the number of ensemble members; and the overbar denotes the ensemble mean. The first term in (3) represents the specified observation error variance. The CR is a ratio of the total variance to mean squared error and gives a measure of how the ensemble prior analysis spread compares to the typical ensemble error, where a value close to 1 is indicative of sufficient ensemble spread for the specified observation error (Dowell et al. 2004; Wheatley et al. 2012).

Differences between the control and MPEX forecasts on the 3-km grid are assessed through their depictions of simulated composite, or column-maximum, reflectivity (referred to as reflectivity hereafter for simplicity) and are quantified by computing differences in fractions skill scores (FSS; Roberts and Lean 2008). Following Schwartz et al. (2010), the computation of FSS uses neighborhoods around the grid cells to give credit to forecasts of storms that may not overlap with, but are close to, the location of observed storms. Numerous neighborhood sizes were tested but results for a neighborhood radius of 20 km are presented here as they are deemed to be representative of the

Brought to you by NOAA Central Library | Unauthenticated | Downloaded 09/22/21 06:55 PM UTC

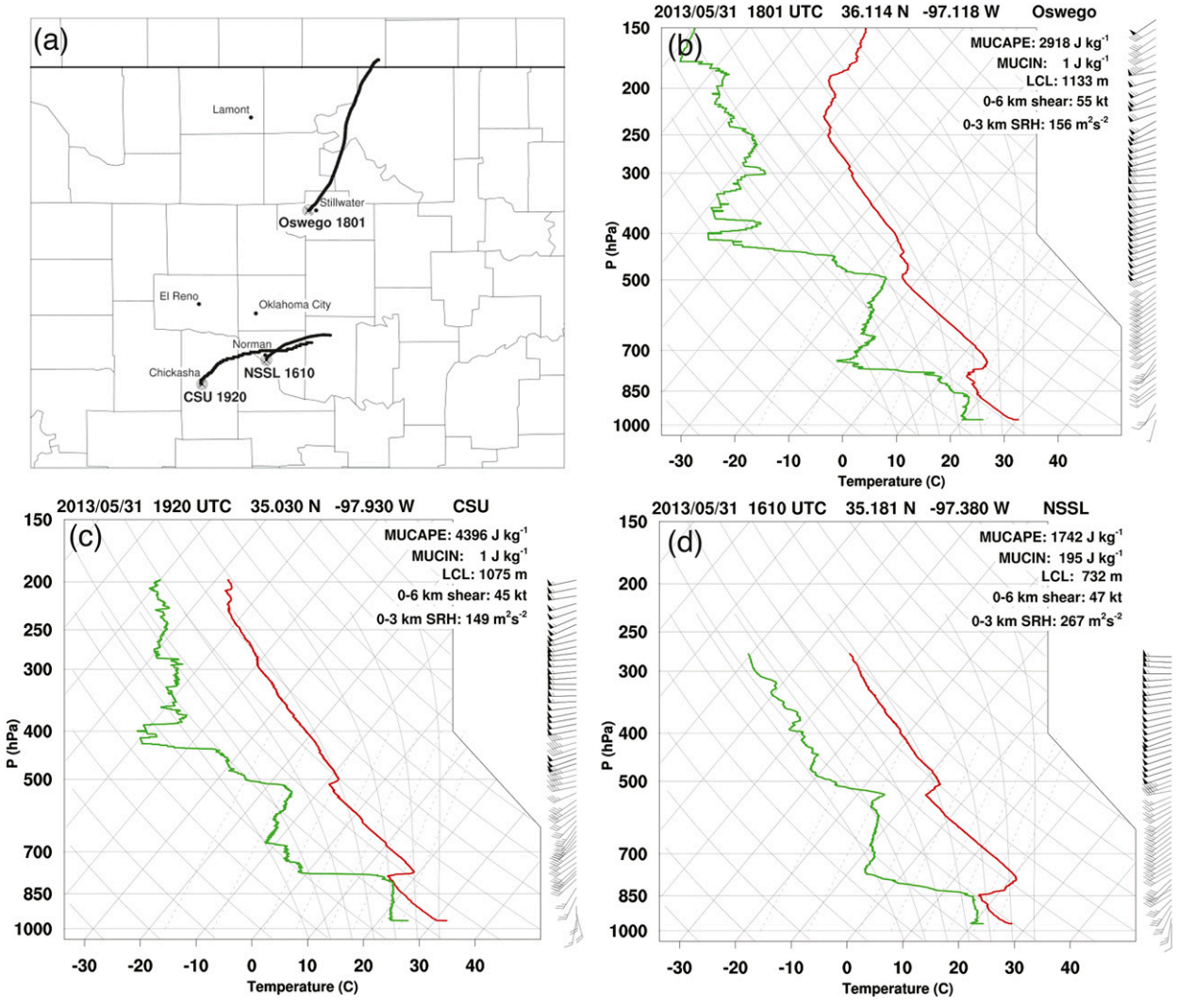

FIG. 6. (a) Locations, launch times (UTC), and trajectories of the three MPEX soundings. Locations referred to in the text are shown. Skew T–log$p$ diagrams for (b) Oswego, (c) CSU, and (d) NSSL are shown with temperature (red) and dewpoint (green). Also shown are variables commonly used in severe weather forecasting computed from the soundings, including the convective available potential energy, convective inhibition, and lifting condensation level (LCL) from the parcel with the largest equivalent potential temperature in the lowest 300 hPa (MUCAPE, MUCIN, and LCL, respectively), the vector wind difference between 10 m and 6 km AGL (0–6-km shear), and the storm-relative environmental helicity between 10 m and 3 km AGL (0–3-km SRH).

subjectively determined difference in skill between the two runs. Furthermore, a radius of 20 km effectively minimizes the penalty from errors on the smallest resolvable scales of the grid ($\leq \sim 4 - 6\Delta x$) in which convective forecasts are not expected to have skill beyond an hour or so (Murphy and Epstein 1989; Zhang et al. 2007; Cintineo and Stensrud 2013). FSS values range from 0 (no skill) to 1 (perfect), but the absolute values of FSS are less important in this application than how the FSS compares between the experiments as the goal is to determine how forecast skill differs from the control experiment.

3. Results

a. *Ensemble evaluation*

Time series of the bias, RMSE, total spread, and CR were computed using assimilated METAR observations. Vertical plots of the same measures for 1200 UTC NWS radiosonde profiles were also computed to provide an overview of the stability of the ensemble and success of the assimilation. Statistics for both prior analysis (forecasts) and posterior analyses are included on the accompanying figures giving the time series trends a characteristic sawtooth shape. Table 3 gives the number

Brought to you by NOAA Central Library | Unauthenticated | Downloaded 09/22/21 06:55 PM UTC

TABLE 2. Localization sensitivity experiments.

Expt	Horizontal cutoff (km)	Vertical cutoff (km)
Default (MPEX)	230	4
doubleloc	460	4
halfloc	115	4
novert	230	20
halfvert	230	2

of METAR, NWS radiosonde, and MPEX observations available and the number of those assimilated.

The ensemble has a small cool and moist bias (~0.5 K) compared to the METAR surface observations over the 3-km domain (Fig. 8). There is also a small ($\sim+0.5\,\mathrm{m\,s^{-1}}$) bias in east–west wind (U) and north–south wind (V). The same comparison using mesonet observations also show a slight cool/moist bias and a positive V bias (not shown). The spike in all plotted fields at 1830 UTC occurs because relatively few METAR observations happen to fall into this assimilation time window (1816–1845 UTC). Overall, these biases are small and do not appear to be detrimental to the overall ensemble given CRs that hover mostly between 1 and 1.5 for all variables.

Statistics are computed for the NWS soundings assimilated at 1200 UTC to examine the quality of the ensemble above the surface. The NWS soundings are interpolated every 25 hPa and statistics are computed across observations at each of these levels. Above the surface, bias is near zero everywhere on the temperature (T) profile except for a small warm bias between 350 and 250 hPa (Fig. 9). Likewise, U- and V-wind biases are less than $1\,\mathrm{m\,s^{-1}}$ everywhere except at the surface. The moist dewpoint (T_d) bias in lower levels becomes larger with height, as much as 2.5 K between 300 and 400 hPa, echoing similar humidity errors found in past studies (Weisman et al. 2008; Fabry 2010; Coniglio 2012).

The RMSE and total spread increase with height for all variables and reach a maximum between 200 and 400 hPa. The increase in RMSE for T is very slight and the maximum in RMSE and total spread occurs at a slightly lower altitude in the T_d profile. The CR for T is close to or slightly above 1, which reflects the very close RMSE and total spread profiles. The CR for the other variables indicates that at 1200 UTC, the ensemble is slightly underdispersive with values generally between 0.5 and 1.0 in the lower half of the troposphere. While this is not ideal, most values fall in the 0.7–1.3 range characteristic of ensemble systems for similar applications and various observation types (Dowell et al. 2004; Wheatley et al. 2012, 2014, 2015) and the ensemble was still accurate and diverse enough that most available observations were assimilated (Table 3). Furthermore,

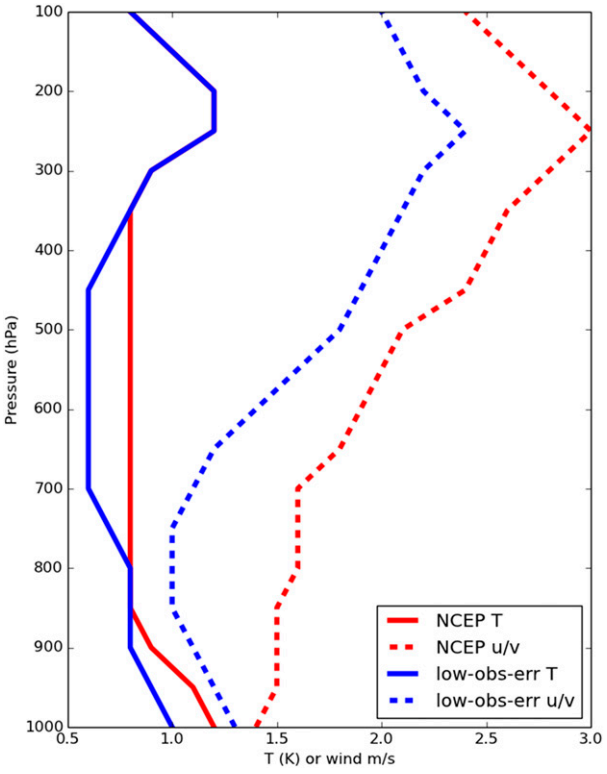

FIG. 7. NCEP default (red) and this study's experimental (low-obserr) (blue) temperature (solid) and wind (dashed) specified observation error standard deviation.

the ensemble goes through 4 more cycles before any MPEX sondes are assimilated and 11 more cycles total before the start of the 3-km forecasts. Tests with assimilation of afternoon MPEX radiosondes for additional cases show that the CR for these variables increases closer to 1 with these additional cycles (not shown).

b. Assimilation impacts

The differences between the control run and MPEX run were examined first through inspection of posterior analysis difference plots between the ensemble mean of the relevant model sounding in the vicinity of the assimilated MPEX sounding 30 min after the start of the

TABLE 3. Assimilation success rate.

Observation type	No. available	No. assimilated	% Success
METAR (full domain)	1 117 483	1 085 061	97.1%
METAR (limited domain)	23 236	21 697	93.4%
NWS radiosonde	54 571	51 447	94.3%
MPEX radiosonde	107	99	92.5%

Brought to you by NOAA Central Library | Unauthenticated | Downloaded 09/22/21 06:55 PM UTC

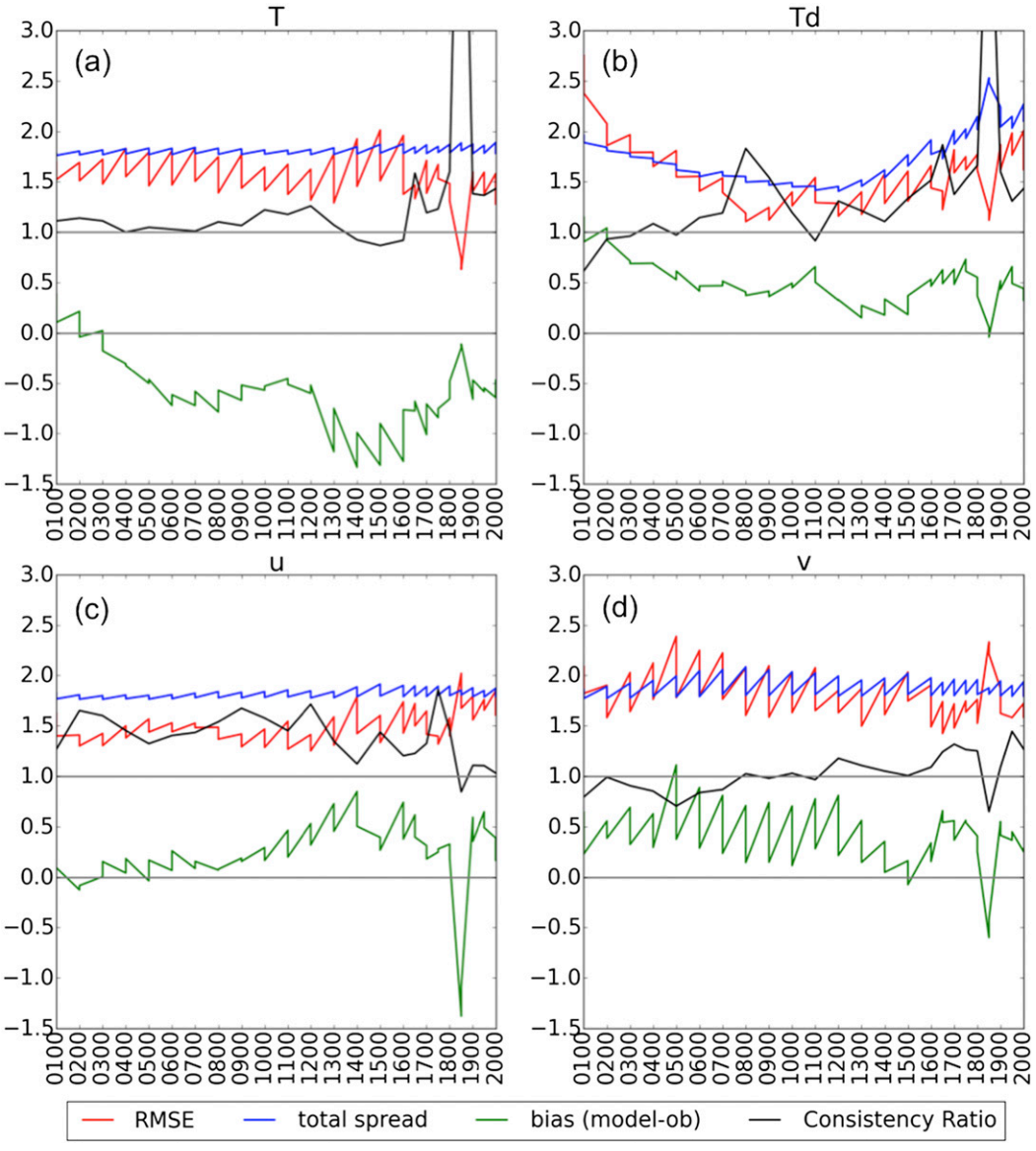

FIG. 8. Time series of RMSE, total error, bias, and consistency ratio (CR) for forecasts (prior analysis) and analyses (posterior) against METAR observations of (a) 2-m temperature (K), (b) 2-m dewpoint (K), (c) 10-m east–west wind (m s^{-1}), and (d) 10-m north–south wind (m s^{-1}) over the 3-km domain. The valid time (UTC) of the forecasts and analyses is along the abscissa. There were over 700 (total, for the four variables shown) observations available over the limited domain at each time during the hourly assimilation cycles and over 250 observations available during half-hourly assimilation cycles, except at 1830 UTC (the spike in fit), when there were only 65 total observations available.

assimilation time. The model sounding profile takes the drift of the sonde into account by computing model fields along a radiosonde trajectory by approximating the path a radiosonde would take through the model fields for each ensemble member. Overall, the largest adjustments were seen in midlevel moisture and zonal (u) wind profiles. However, substantial adjustments were also seen in the temperature profiles near the top of the boundary layer (~800 hPa). Near-surface adjustments were small in T and T_d due in part to the small differences between the observations and the ensemble mean prior analysis, and the relatively small ensemble spread (Figs. 10 and 11).

As expected, the ensemble spread decreases nearly everywhere in the MPEX run, and the ensemble means shift toward the observations. The largest of these shifts

Brought to you by NOAA Central Library | Unauthenticated | Downloaded 09/22/21 06:55 PM UTC

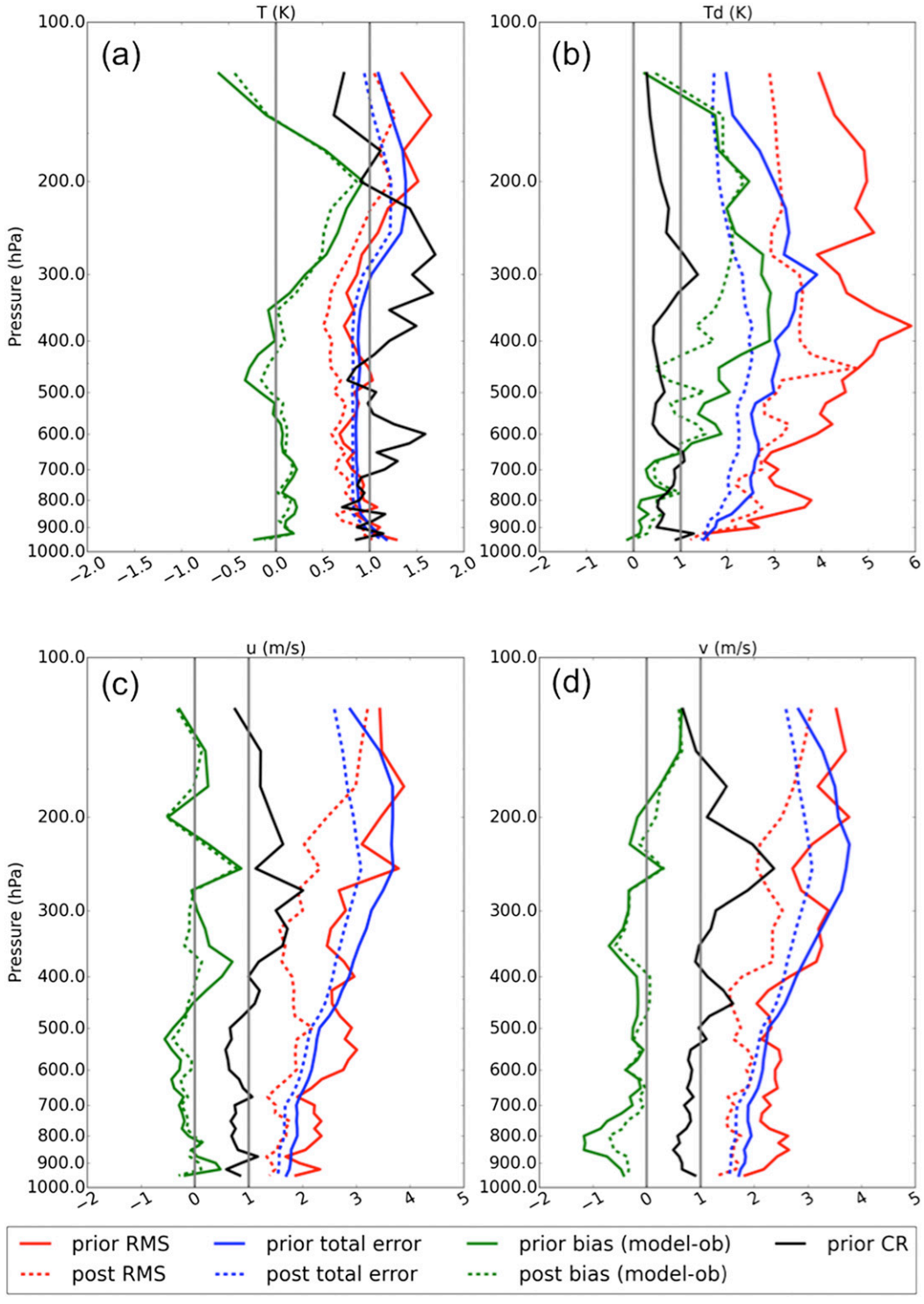

FIG. 9. Vertical profile of RMSE, total error, bias, and consistency ratio (CR) for forecasts (prior analyses) and analyses (posterior) against 1200 UTC NWS sounding observations of (a) temperature (K), (b) dewpoint (K), (c) east–west wind ($m\,s^{-1}$), and (d) north–south wind ($m\,s^{-1}$).

Brought to you by NOAA Central Library | Unauthenticated | Downloaded 09/22/21 06:55 PM UTC

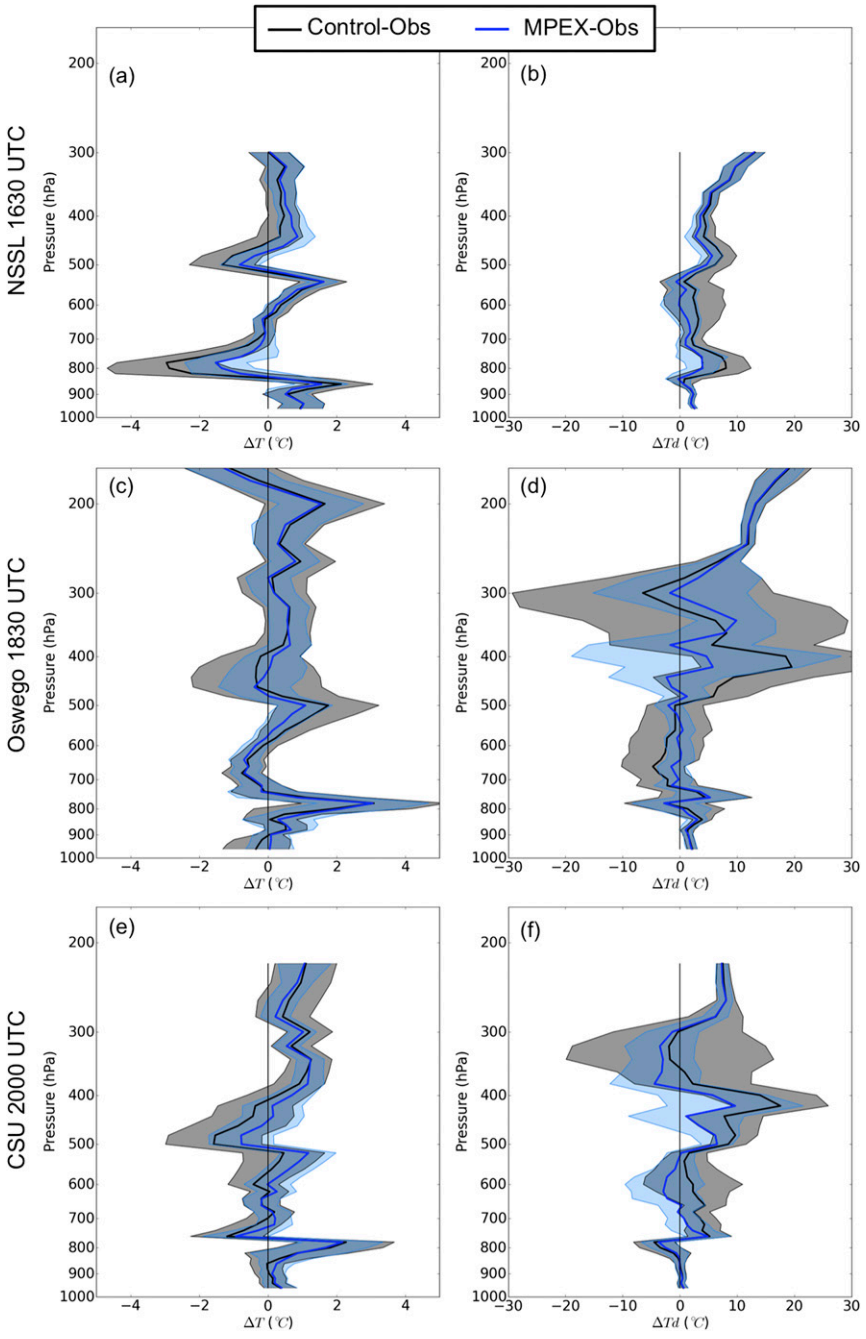

FIG. 10. Ensemble mean difference between model posterior analysis and relevant sounding for control (black) and MPEX (blue) runs valid for (a),(b) 1630 UTC for a launch starting location near the NSSL sounding; (c),(d) 1830 UTC near the Oswego sounding; and (e),(f) 1930 UTC near the CSU sounding. (left) T and (right) T_d. The shaded regions represent $\pm 3\sigma$ to illustrate the ensemble spread.

occur in T_d between ~800 and 400 hPa, where the control run had the largest differences and largest spread. The end result of these changes is drying between ~750 and 350 hPa in the vicinity of the NSSL and CSU soundings, and midlevel (~750–500 hPa) moistening and upper-level (~500–350 hPa) drying in the vicinity of the Oswego sounding.

Similarly, the MPEX run indicates a decrease in zonal wind speed around ~900–550 hPa in the vicinity of the NSSL launch and a decrease in zonal wind speed

Brought to you by NOAA Central Library | Unauthenticated | Downloaded 09/22/21 06:55 PM UTC

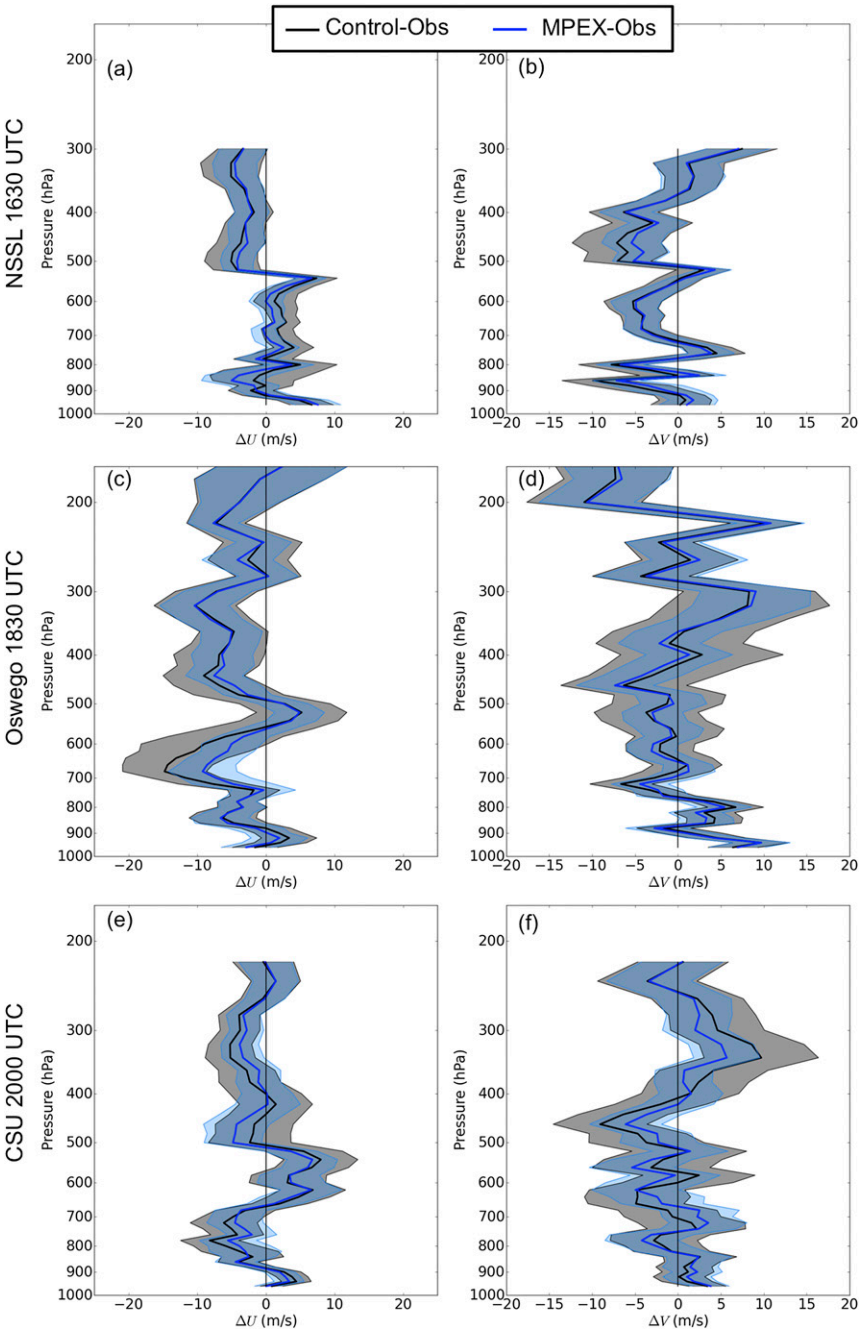

FIG. 11. As in Fig. 10, but for (left) U and (right) V in kt.

between ~750 and 550 hPa near the Oswego launch (Figs. 11b,d). Slight decreases in near-surface zonal wind were also seen in the Oswego and CSU launches.

Although the changes in T are smaller than the changes in T_d, the mean of the MPEX run fits the T profile of the capping inversion in the NSSL sounding (Fig. 6d) near 800 hPa better than in the control run (Fig. 10a). Near the secondary inversion around 525 hPa, the posterior analysis for the MPEX run fits the T profile a little better than the control run in the vicinity of all three launches (Figs. 10a,c,e), but the relatively coarse model vertical resolution at that level hinders a closer fit to the observation.

Near the surface, the T forecasts (prior analyses) were very close to the observed values near the ground (mean differences are ~0.3–0.6 K), and the ensemble spread in

Brought to you by NOAA Central Library | Unauthenticated | Downloaded 09/22/21 06:55 PM UTC

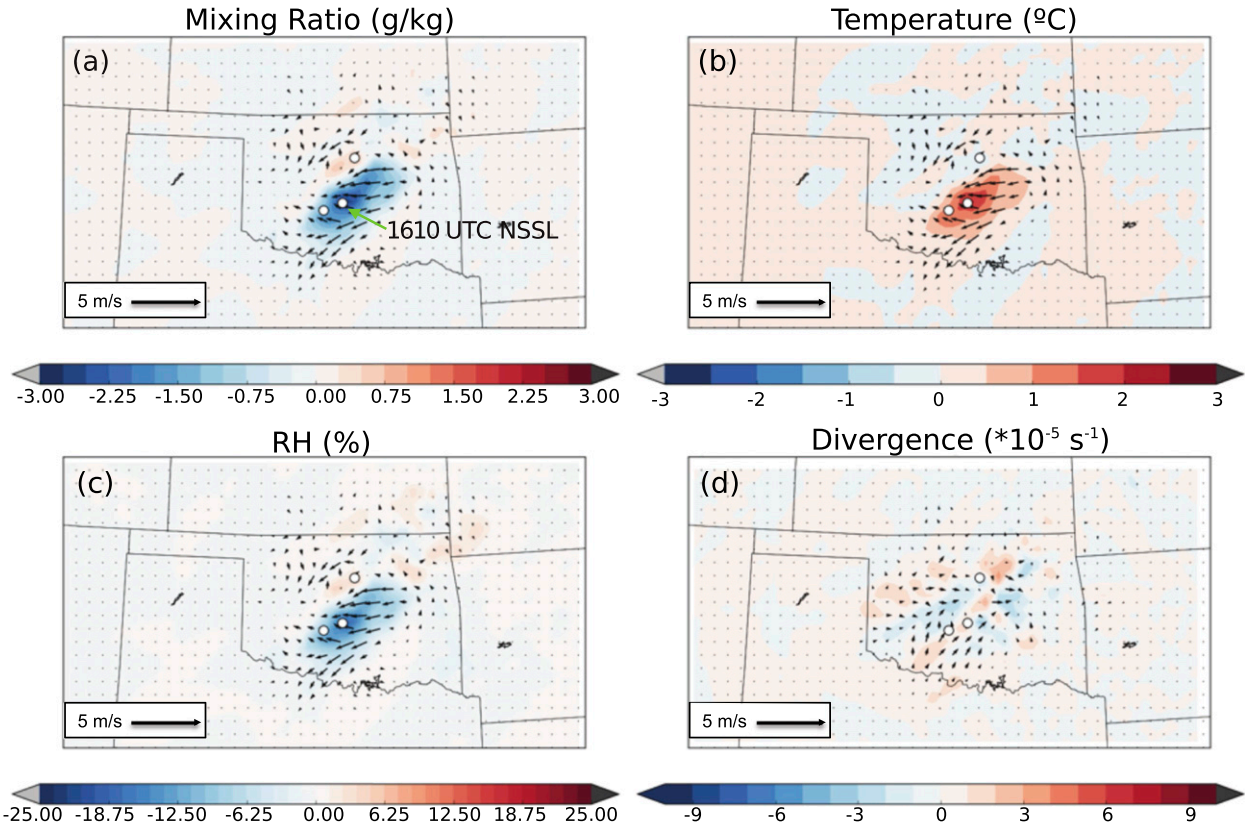

FIG. 12. Model posterior analysis differences (MPEX − control) at 1630 UTC at model level 11 (just above the top of the boundary layer) for (a) water vapor mixing ratio (g kg^{-1}), (b) temperature (°C), (c) relative humidity (%), and (d) divergence ($\times 10^{-5}$ s^{-1}) at model level 6 (~900 hPa). Vectors represent wind differences (MPEX − Control) at the same model level as each variable. The green arrow points to the location of the 1610 UTC NSSL sounding.

T was small (standard deviation, or σ, of ~0.25–0.5 K), thus the ensemble mean T changed very little upon the assimilation of the MPEX soundings. When the spread is small relative to the specified observation error as in this case, along with a relatively small difference between the prior analysis (forecasts) and observations, the Kalman gain will be small (Snyder and Zhang 2003). The T_d in the lowest 500 m above ground level (AGL) in all three soundings also changed very little because the prior ensemble T_d spread was small ($\sigma \sim$ 0.3–0.5 K), which prevented the assimilation from correcting the low-level moist bias (~1.5–2 K) seen near the soundings.

Horizontal plan views of the thermodynamic and kinematic fields above the surface help give an understanding of how the assimilation influences model points away from the sounding location (Fig. 12). The drying and warming near the inversion seen in Fig. 10a can also be seen in the posterior analysis in a coherent mesoscale pattern at distances over 200 km away (Fig. 12a). These both contribute to as much as a 15% decrease in RH (Fig. 12c). The weakening of the west-southwesterly flow at about 1–2 km AGL near the NSSL sounding (Fig. 11a) also extends downstream in roughly the same area of the RH adjustments. The coherent mesoscale pattern in these adjustments shows some of the benefits of using a EAKF technique—the flow-dependent covariances create an elliptical region of adjustments in roughly the same orientation of the frontal boundary and mean low- to midlevel flow, which is biased somewhat downstream of the sounding location. Although the adjustments to the winds are small, they do result in a somewhat more convergent region near the frontal boundary in southwest Oklahoma at this time (Fig. 12d) along with slightly stronger southerly low-level flow just to the east of the dryline.

Over time, the impacts of the individual soundings are more complex because of small-scale covariance structures introduced by the sequential assimilation of multiple soundings between 1600 and 2000 UTC (recall that there are three soundings from the operational data stream also being assimilated between 1700 and 1800 UTC). In other words, the impacts of the sounding assimilation are cumulative, as expected, but the

Brought to you by NOAA Central Library | Unauthenticated | Downloaded 09/22/21 06:55 PM UTC

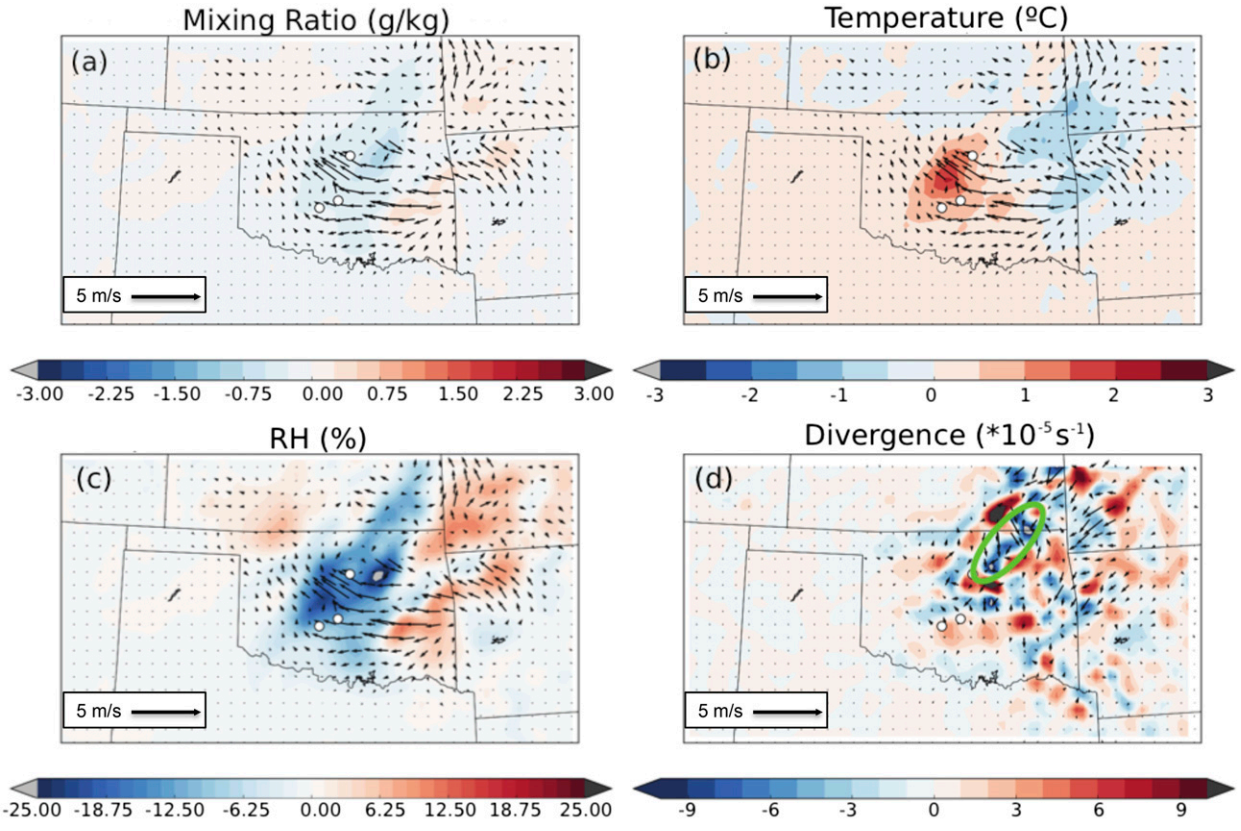

FIG. 13. Model posterior analysis differences (MPEX − control) at 2000 UTC at model level 18 (~500 hPa) for (a) water vapor mixing ratio (g kg^{-1}), (b) temperature (°C), (c) relative humidity (%), and (d) divergence ($\times 10^{-5}$ s^{-1}) at model level 6 (~900 hPa). Winds computed as in Fig. 12. The area outlined in green highlights an area of more convergent low-level flow near the front in the MPEX run referred to in the text.

adjustments result in structure added to the smallest resolvable scales of the grid (~60–90 km) over time. Despite this increasing complexity to the differences between the control and MPEX runs, there are more areas of low- to midlevel warming and drying than there are regions of cooling and moistening downstream of the launch locations (Fig. 13). This is particularly evident around 500 hPa where the RH is over 20% lower over much of central Oklahoma at 2000 UTC (Fig. 13c).

The development of smaller mesoscale structure over time results in a rather noisy pattern of low-level divergence (Fig. 13d). However, a mesoscale pattern in the difference in low-level divergence between the control and MPEX runs is a southwest–northeast-oriented region of more convergent low-level flow in northern Oklahoma into southeast Kansas with surrounding bands of more divergent low-level flow. This banding is associated with the frontal boundary and is an indication that the assimilation of the MPEX soundings results in a sharpening of the kinematic component of the front in this region (Fig. 2a).

In summary, the assimilation of the MPEX soundings has a noticeable mesoscale impact on the ensemble mean analysis. In particular, the largest cumulative effects of assimilating the three soundings are to warm and dry the low- to midlevels, mostly downstream of the launch locations. While the adjustments to the winds are relatively small, they result in a sharpened, more convergent low-level frontal boundary over northern Oklahoma and southeast Kansas. The following section examines the differences that arise between two ensembles of convection-permitting (3 km) forecasts: one that is initialized from the ensemble of control run analyses valid at 2000 UTC and the other initialized from the MPEX run analyses valid at the same time.

c. *Convection-permitting forecasts*

The differences between the control and MPEX 3-km forecasts are best illustrated by probabilities (or relative frequencies) of ensemble members that have reflectivity ≥40 dBZ within 20 km of each grid cell (that are then smoothed slightly with a Gaussian weighting

Brought to you by NOAA Central Library | Unauthenticated | Downloaded 09/22/21 06:55 PM UTC

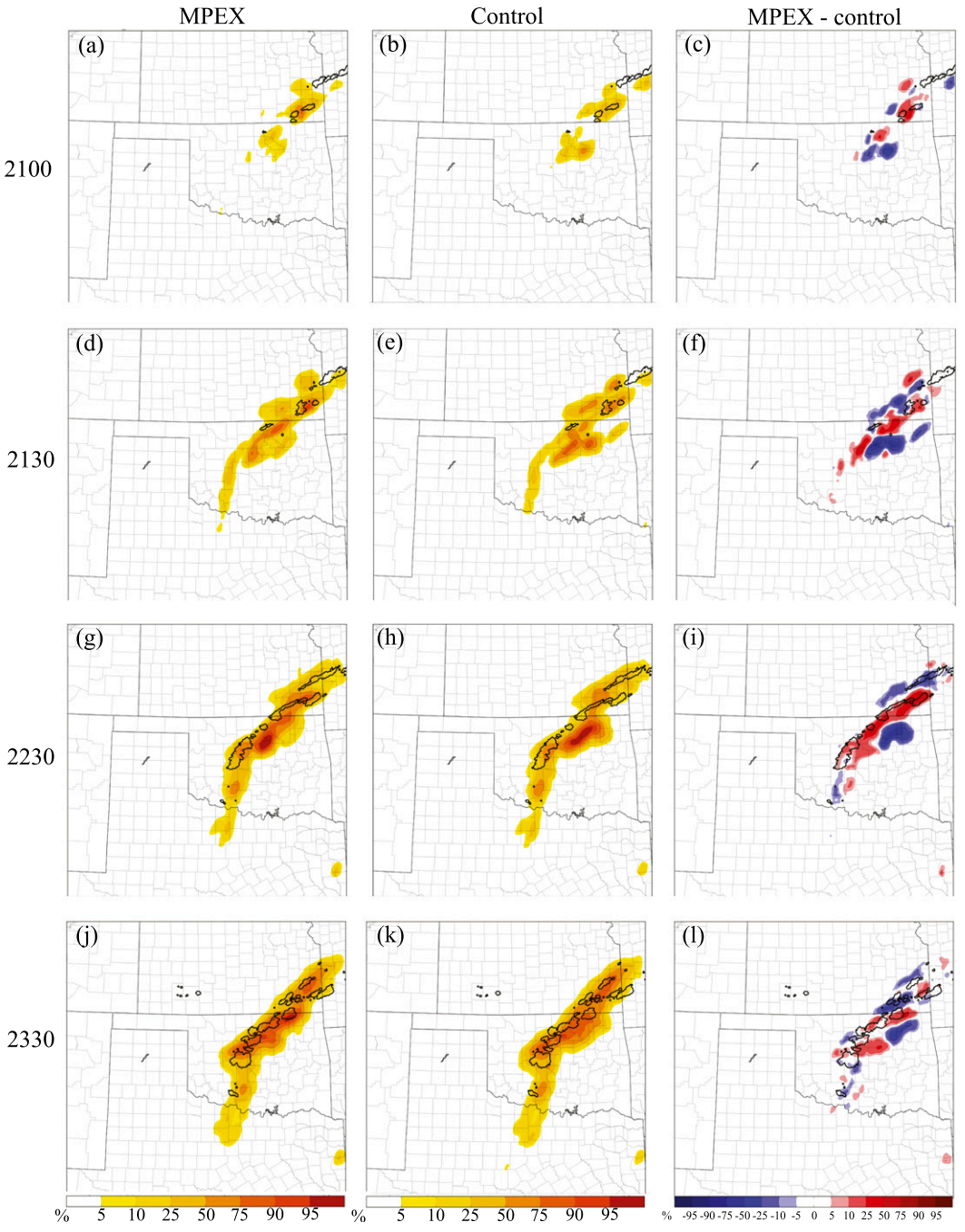

FIG. 14. Smoothed probability of reflectivity ≥40 dBZ within 20 km of a grid cell for (left) MPEX, (middle) control forecasts, and (right) their difference valid at (a)–(c) 2100 UTC (1-h forecast), (d)–(f) 2130 UTC (1.5-h forecast), (g)–(i) 2230 UTC (2.5-h forecast), and (j)–(l) 2330 UTC (3.5-h forecast) 31 May 2013. In the rightmost column, red (blue) areas denote higher (lower) reflectivity probabilities for the MPEX run. Black contours outline observed reflectivity ≥40 dBZ from the NSSL National Mosaic and MultiSensor Quantitative Precipitation Estimates system (Zhang et al. 2011).

function with a σ of the Gaussian kernel of 2) (Figs. 14 and 15). By 2100 UTC (1-h forecast), the MPEX run initiates fewer storms over northeastern Oklahoma where storms were not observed and initiates more storms over far southeastern Kansas where storms were observed (Fig. 14). In the MPEX run, the spurious storms that develop over northeastern Oklahoma are fewer in number and develop closer to where the

Brought to you by NOAA Central Library | Unauthenticated | Downloaded 09/22/21 06:55 PM UTC

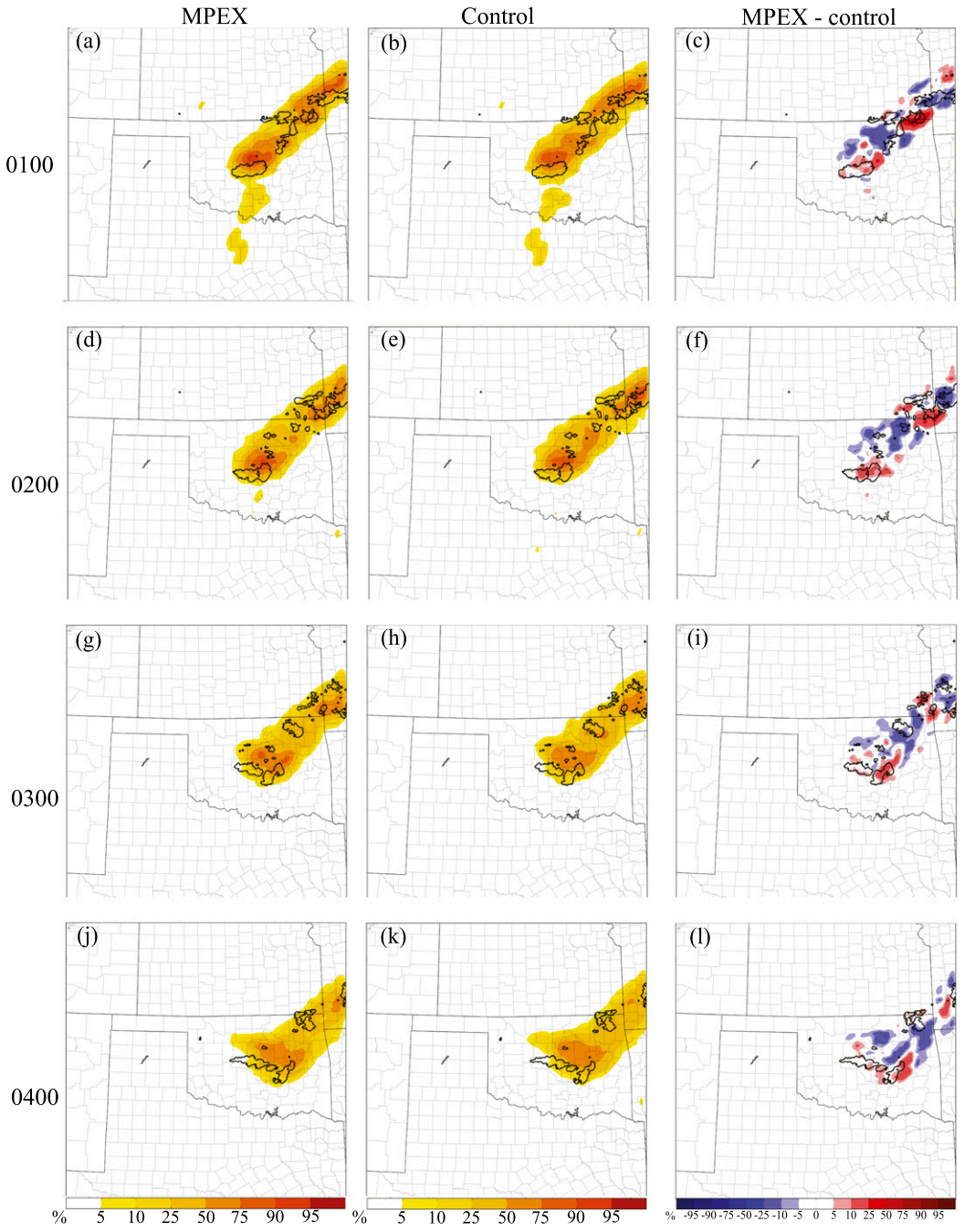

FIG. 15. As in Fig. 14, but for forecasts valid at (a)–(c) 0100 UTC (5-h forecast), (d)–(f) 0200 UTC (6-h forecast), (g)–(i) 0300 UTC (7-h forecast), and (j)–(l) 0400 UTC (8-h forecast) 1 Jun 2013.

observed storms just begin to develop. Between 2100 and 2230 UTC, additional storms initiate along the front from southeastern Kansas into central Oklahoma in both runs (Figs. 14d–i). The largest difference between the two runs at 2230 UTC is over northeastern Oklahoma (Fig. 14i) where the over initiation of spurious storms in the control run by 2100 UTC led to an overabundance of storms (the blue area in northeastern Oklahoma in Fig. 14i). Furthermore, the tendency for storms to develop closer to the front in the MPEX run leads to higher concentration of storms closer to where they are observed from central Oklahoma into southeastern Kansas by 2230 UTC (the red southwest–northeast-oriented band that nearly overlaps the black contours in northern Oklahoma in Fig. 14i).

Brought to you by NOAA Central Library | Unauthenticated | Downloaded 09/22/21 06:55 PM UTC

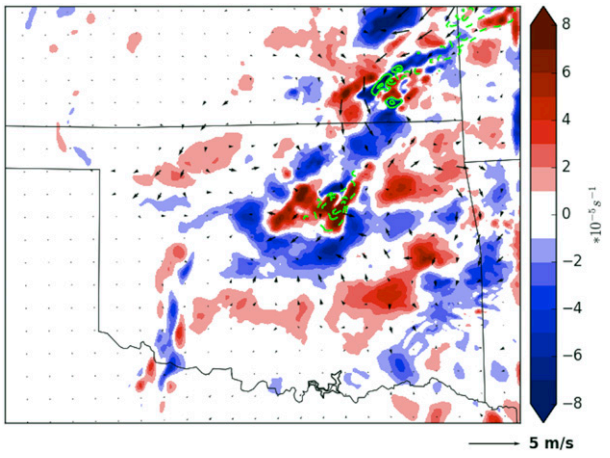

FIG. 16. Ensemble mean difference (MPEX − Control) of divergence ($\times 10^{-5}$ s^{-1}; filled contours) and cloud water mixing ratio (g kg^{-1}; unfilled green contours) averaged over the first 30 min of the nested grid forecast, covering the initial CI period. Divergence is averaged over layers 4–10 (~950–820 hPa), and the cloud water mixing ratio was averaged over ~750–450 hPa. Contours of cloud water mixing ratio range from 1 to −1 g kg^{-1}, and dashed contours are negative. Arrows represent MPEX − Control wind differences averaged over the same parameters as the divergence field.

Inspection of the forecasts in the first hour shows that fewer storms develop in the MPEX forecasts away from the front in northeastern Oklahoma partly because of the shifting of the low-level convergence/divergence patterns (Fig. 13d), and partly because of entrainment of drier air into the nascent convection in the MPEX run (Fig. 13c), which prevents more storms from fully developing in this region. This can be seen by a region of higher cloud water mixing ratio in the control run at 30 min (indicated by the region of dashed green contours) collocated with enhanced convergence in the control run in northeast Oklahoma (Fig. 16).

As evidenced by the lower-level wind field differences averaged over the first 90 min of the forecasts (Fig. 17b), the MPEX run has larger southerly and easterly components in the region of the early CI in the control run. These stronger southeasterlies in the MPEX run results partly from the early convection in the control run producing a cold pool, which acts to reduce convergence west of the CI in the control run. Therefore, the enhancement in convergence closer to the front in the MPEX forecasts (Fig. 17) results from a combination of the preconvective mesoscale adjustment to the convergence (Fig. 13d), and the disruption of the southeasterlies in the control run from the spurious convection. This enhanced convergence closer to the front in the MPEX forecasts leads to the higher concentration of storms closer to where they are observed from central Oklahoma into southeastern Kansas by 2230 UTC (Fig. 14i).

One of the forecast challenges on this day was determining the southern extent of sustained convection along the dryline in southwestern Oklahoma (Fig. 2). Convection initiated there by 2230 UTC, but it was relatively short lived (Fig. 2). The impact of the MPEX soundings in this area was minimal as both runs develop too much convection along the dryline and too far south into northern Texas where storms never developed (Figs. 14g–l). This is a reflection of the tendency for the model adjustments by the MPEX soundings to be focused downstream (relative to the low- to midlevel winds) of the sounding locations.

By 2330 UTC, the differences between the MPEX and control forecasts become noisier and it is difficult to identify clear improvements in the MPEX reflectivity forecasts (Figs. 14j–l). This indicates that from about 2330 to 0030 UTC, the impact of the soundings on the convective-scale forecasts over the domain is small. However, the impact does not appear to diminish everywhere over time. From 0100 to 0500 UTC, the MPEX run has consistently higher probabilities than the control run near the southernmost collection of cells in central Oklahoma and has consistently lower probabilities in northeastern Oklahoma where few storms were observed in this period (Figs. 15a–i). The southernmost storms that appear to be handled better in the MPEX run in this period are those that consolidated from the cluster of supercells that produced the tornadoes near El Reno earlier, grew upscale, and surged eastward into east-central Oklahoma by 0400 UTC (Fig. 3). Elsewhere, through the end of the forecast, both runs produce the west-northwest–east-southeast-oriented line of back-building storms too far north relative to the observed back-building storms over central Oklahoma. This indicates that, like for the earlier dryline storms in southwest Oklahoma, the impact from assimilation of the MPEX soundings on the mesoscale heavy-rain event over central Oklahoma was minimal (Fig. 15), perhaps because of the accumulation of model error by this time in the forecast and because the adjustments to the analyses had moved downstream out of the area by this time.

To better quantify the differences in reflectivity forecasts, the FSS was computed for reflectivity ≥40 dBZ at a variety of neighborhood radii. (Shown in Fig. 19a are the differences between the MPEX FSS and the control FSS for a 20-km neighborhood radius to be consistent with the radii used for computing and displaying the reflectivity probabilities.) Figures 18 and 19 include 95% confidence intervals following Hamill (1999) with the ensemble members in each run serving as the samples (assuming independence among the ensemble members). As suggested by the analysis of the neighborhood probability differences, the most

Brought to you by NOAA Central Library | Unauthenticated | Downloaded 09/22/21 06:55 PM UTC

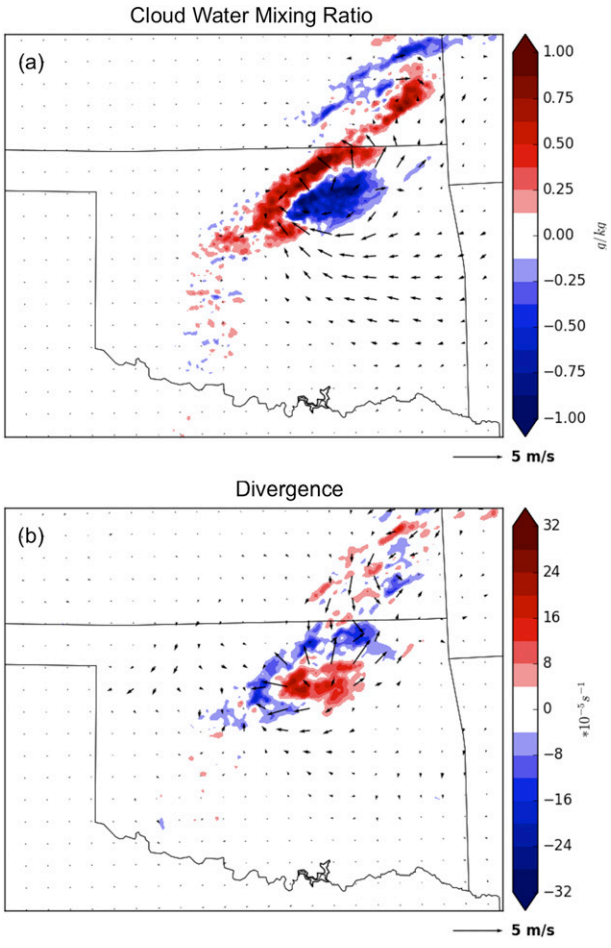

FIG. 17. Ensemble mean difference (MPEX − Control) of (a) cloud water mixing ratio (g kg^{-1}; red areas indicate more cloud water in the MPEX experiments) and (b) divergence ($\times 10^{-5}$ s^{-1}; blue areas indicate more convergence in the MPEX experiments). Layer averages were computed as in Fig. 16. As in Fig. 16, vectors represent wind differences, averaged over the same layers as the variable displayed in each subfigure.

significant improvements in FSS for the MPEX run occur in the first three hours of the forecasts. This improvement in FSS is a reflection of the MPEX run both delaying the development over spurious storms ahead of the front in northeastern Oklahoma and having higher probabilities of storms closer to the front (Fig. 14). At later times, the FSS differences support the subjective assessment of the probability differences shown earlier that the two ensembles of forecasts become very similar in skill in the 2330–0030 UTC time period, and that the MPEX forecasts are somewhat better in skill in the period after 0200 UTC. However, the confidence intervals widen considerably and overlap with zero after 2315 UTC owing to the growing spread in the location of the storms, which lowers the ability to confidently say the MPEX forecasts were collectively better after this time.

d. Sensitivity tests

In the first part of the sensitivity experiments, runs excluding special 1700/1800 UTC NWS soundings were produced to better understand the impact of the MPEX soundings. FSS as described in the previous paragraph was computed for the difference between the control run and the run with no MPEX soundings or NWS special soundings (NONWS), and for the difference between the MPEX run that excluded the NWS special soundings (MPEX-NONWS) and NONWS (Fig. 18). The differences were computed such that the run with less assimilated information was subtracted from the run with more assimilated information in each case.

In the Control-NONWS comparison, differences in FSS were small and lacked statistical significance at all times (Fig. 18b). This indicates that the collective effects of the 1700 UTC sounding from Lamont, Oklahoma; the 1800 UTC sounding from Norman, Oklahoma; and the 1800 UTC sounding from Springfield, Missouri; had much less impact on the forecasts than assimilating the additional three MPEX soundings. The FSS for the experiment that only assimilated the MPEX soundings and not the NWS soundings (MPEX_NONWS-NONWS) was generally greater than those of the run that assimilated neither the MPEX nor the NWS soundings, but the FSS jumped around from one time to the next, especially in the early part of the forecast. There were five times that were significant between 2000 and 2245 UTC, two positively and two negatively. This indicates that the assimilation of the MPEX soundings had the largest impact on the forecasts when the NWS soundings were also included in the assimilation.

A number of additional experiments were performed to examine the sensitivity of the results to changes in parameters used in the assimilation as described in section 2b. Differences in FSS between these experimental runs and the control run show that the experiment that cuts the horizontal localization in half (hlafloc) is the most skillful very early in the forecast, peaking near 2045 UTC (Fig. 19b), largely because it spins up the few storms over far southeastern Kansas prior to 2100 UTC in approximately the right place and time, and has the fewest number of spurious storms in northeastern Oklahoma (not shown). However, the halfloc run becomes much closer in skill to the control run shortly thereafter (Fig. 19b). The halfloc run remains more skillful than the control run throughout the entire forecast, but a widening spread, seen in all runs, lowers statistical significance after the first hour.

Brought to you by NOAA Central Library | Unauthenticated | Downloaded 09/22/21 06:55 PM UTC

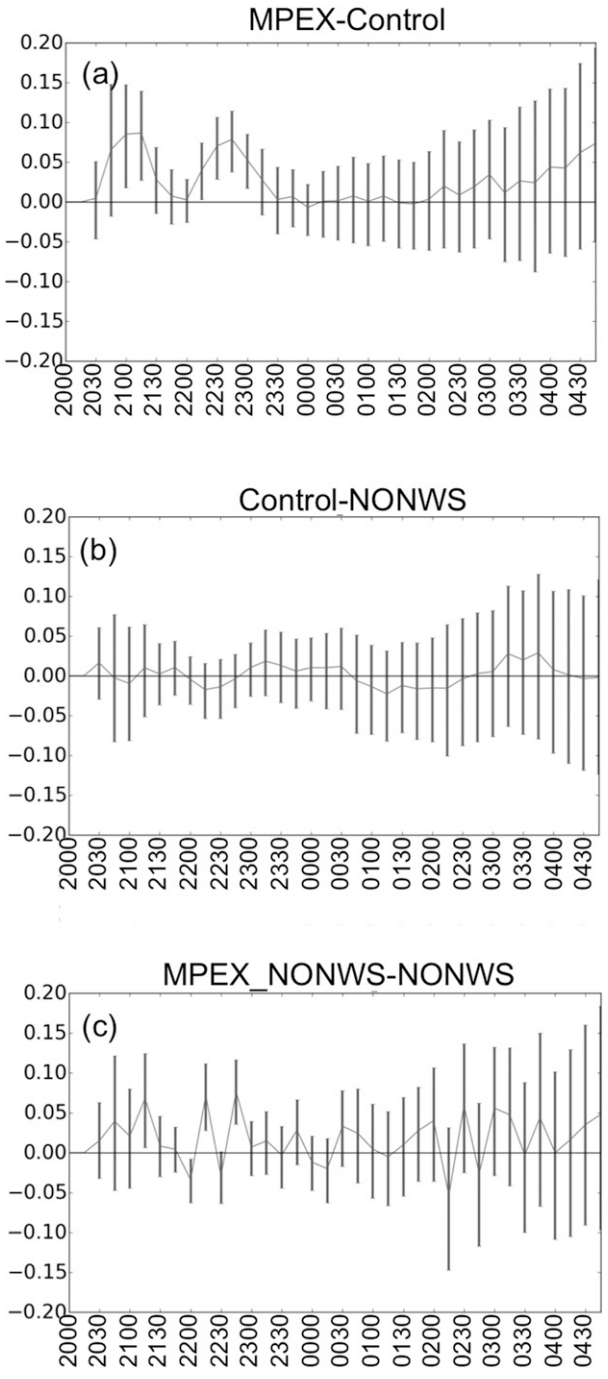

FIG. 18. Difference (experiment − control) of FSS and 95% confidence intervals for the (a) MPEX, (b) NONWS, and (c) MPEX_NONWS forecasts. The valid time (UTC) of the forecasts is along the abscissa.

The doubleloc run shows the opposite behavior by becoming more skillful than the control run after 2100 UTC, peaking around 2200 UTC, and staying more skillful than the control run through 2300 UTC (Fig. 19e). The MPEX run contains the individual significant skill improvements over the control run seen in the halfloc and doubleloc runs at both of these peaks around 2045 and 2200 UTC, although the magnitude of the FSS differences in each peak in the MPEX run are not as large as those seen in the halfloc and doubloc runs.

In general, altering the vertical localization cutoff radius from a value of 4 km had a detrimental impact on the first few hours of the forecasts (Figs. 19c,f). The halfvert run was less skillful than the control run early in the forecast but became increasingly similar to the control run as the forecast progressed, except for a very short period around 0100 UTC. The novert run varied in skill compared to the control run throughout the forecast, and the differences only had one very brief period approaching statistical significance—between 2115 and 2145 UTC—but generally showed similar or inferior forecasts compared to the control run.

Finally, the lowobserr experiment showed very similar trends compared to the MPEX run with two periods of statistically significant improvement in skill over the control run early in the forecast period (Fig. 19d). Unlike the MPEX run, the FSS for the lowobserr run became smaller than that for the control run over time. This suggests that the procedure of binning the observations into half-hourly windows and assimilating the true position of the sonde (i.e., taking balloon drift into account) is not justification to lower the specified observation error for this application since the differences between the MPEX and lowobserr runs are small in the first few hours of the forecasts when we can have confidence in the differences between the runs.

4. Summary and conclusions

This study examines the impact of assimilating three balloon-borne radiosonde profiles that were obtained from mobile facilities as part of the MPEX field program on an ensemble of mesoscale analyses and forecasts of the significant convective event on 31 May 2013 over Oklahoma. The goal is to determine if the changes to the mesoscale analyses resulting from the assimilation of these soundings using an ensemble Kalman filter method improves short-term convection-permitting forecasts of the event driven by these analyses.

Exploration of the prior analysis (forecasts) and posterior analysis with and without the assimilation of the MPEX soundings on the mesoscale grid shows that the MPEX soundings make a meteorologically meaningful impact on the model variables above the surface. In particular, despite a small moist bias in the forecasts, moisture has a closer fit to the observed soundings in the MPEX run, especially in the low- to midlevels. This supports the conclusions of Fabry and Sun (2010) and

Brought to you by NOAA Central Library | Unauthenticated | Downloaded 09/22/21 06:55 PM UTC

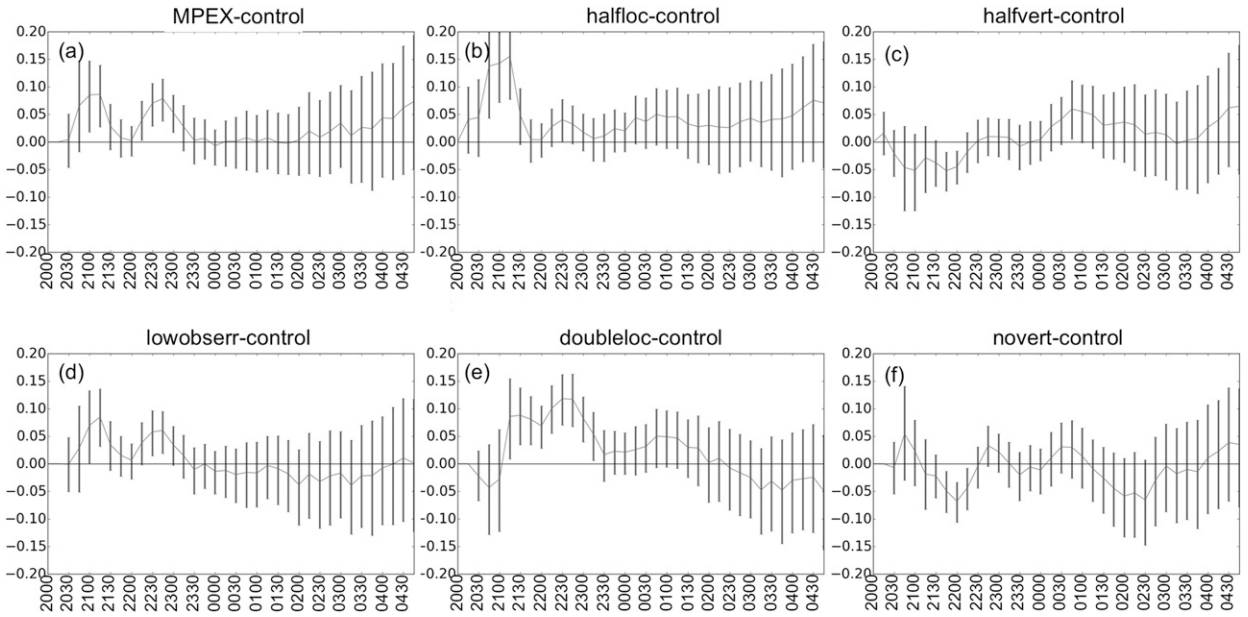

FIG. 19. Difference (experiment − control) of FSS and 95% confidence intervals for the (a) MPEX, (b) halfloc, (c) halfvert, (d) lowobserr, (e) doubleloc, and (f) novert forecasts. The valid time (UTC) of the forecasts is along the abscissa.

Fabry (2010) regarding the potential benefits of radiosonde assimilation for improving predictions of low- to midlevel moisture and the subsequent improvements in the mesoscale short-term prediction of convective precipitation. There are also slight improvements in the analysis fit to the observed low-level temperature profiles near the top of the boundary layer, particularly near the capping inversion. Adjustments to the winds were mostly small, and limited to low levels, but the collective effects of the assimilation resulted in more convergence closer to the observed location of a frontal boundary in northern Oklahoma and southeastern Kansas.

The changes to the analysis that resulted in a better fit to the observations were not limited to a region very near the sounding location. Rather, the adjustments could be seen over mesoscale areas and were concentrated downstream of the sounding launch location. Forecasts from times after the assimilation indicate that the changes to the analyses seen in the vertical profiles of the variables, especially moisture, persist in subsequent forecasts and analyses although the patterns of the adjustments and differences between the MPEX and control runs become noisier over time.

The assimilation of the MPEX soundings had a noticeable positive impact on the forecasts of convection, mainly during the first three hours of the forecast. In the MPEX run, the initiation of spurious storms in northeastern Oklahoma away from the front was reduced, and the probabilities of storms that formed after 2100 UTC along and near the front were higher and closer to the observed storms. Inspection of the storm development in the first few hours shows that the increased convergence near the frontal zone in the MPEX run and the lower relative humidity in low- to midlevels in the MPEX run contributed to this improvement. The MPEX run also had somewhat better skill at forecasting the position and timing of the later storms in central Oklahoma after about 0100 UTC although the larger spread in the forecasts prevented a clear determination of the significance of this result. These findings agree with previous sentiments that convection organized on the mesoscale may be predictable for several hours within mesoscale neighborhoods (Weygandt et al. 2004; Kain et al. 2010; Stratman et al. 2013). This study adds that improvements to the mesoscale environment afforded by the assimilation of special radiosonde profiles may increase that mesoscale predictability, at least in the first few hours of the forecasts.

The assimilation of preconvective soundings did not help to reduce the early and overabundant storms along the dryline in southern Oklahoma and northern Texas. The lack of influence on the dryline storms may be due to the location of the MPEX launches. The primary adjustments to the analyses resulting from the assimilation of the MPEX soundings were seen downstream (relative to the low- to midlevel winds) of the launch locations. All of the MPEX launches on 31 May took place east of the dryline and well north of where the storms formed in southwest Oklahoma, so they were

Brought to you by NOAA Central Library | Unauthenticated | Downloaded 09/22/21 06:55 PM UTC

likely to have little influence on the dryline and subsequent convection in this area. Likewise, the assimilation of MPEX soundings did not significantly improve the forecasted location of the later back-building storms over Oklahoma City that contributed to the deadly flash flood. While the MPEX soundings were taken in the vicinity of the subsequent flash flood, they were taken over 6 h earlier and thus the assimilation impacts had diminished in the area over time, while model error increased.

Experiments were performed to test the sensitivity of the results to changes in the configuration of the ensemble data assimilation and the inclusion/exclusion of NWS special soundings. Experiments that only assimilated the three special NWS soundings, and only assimilated the three MPEX soundings showed some improvement over the control run on their own, but when all six soundings were assimilated, significant improvements over the experiment that did not assimilate the MPEX soundings were seen in the first 3 h of the forecast.

While there was not a clear indication that halving or doubling the horizontal localization radius from the default value of 230 km significantly changed the results, there was some impact on the specific times that the assimilation of the MPEX soundings improved convective-forecast skill over the control run. Halving the localization improved the skill in the first hour of the forecast (effectively placing the few initial storms in the early spinup period more accurately), while doubling the horizontal localization produced convective forecasts with better skill for 1–3-h forecasts, but worse skill after about 4 h (although the large spread in forecasts later in the forecast lowers the confidence in this assessment). Likewise, the results did not lend support to using a vertical localization radius different from the default value of 4 km, nor using specified temperature and wind observation errors different from the default NCEP observation error values within DART.

Care must be taken with these results for a number of reasons. This was only one case, and while it seems that additional assimilated soundings do have a positive impact, especially in the first three hours, these procedures need to be repeated for more cases to determine if these findings are consistent among other MPEX cases. An investigation into the impacts of soundings over other MPEX cases is currently under way.

Furthermore, while the bias in the ensemble was relatively small for most variables and levels, there was still some bias in all variables both near the surface and in dewpoint in upper levels. It is possible that the assimilation results could be improved if steps are taken to reduce these biases, and the detrimental effects they can have on the analyses (Ancell 2012; Romine et al. 2013). Furthermore, steps to increase the spread in temperature and dewpoint near the surface beyond what using diversity in turbulence parameterization schemes produced in this study could allow for the assimilation of sounding data to have more impact in low-levels than what was seen in this study.

There were a limited number of special soundings available for this case, and they were not collected with testing data assimilation impacts as the primary goal. The MPEX soundings positively influenced the convective forecasts for this event, but it may be possible to estimate prior to the event happening where the observations should be taken to maximize the impact of the soundings on subsequent forecasts. Studies of meteorological phenomena on synoptic scales have long experimented with choosing the sounding location based on quantitative targeting procedures (e.g., Langland et al. 1999; Hakim and Torn 2008; Torn and Hakim 2008; Gelaro et al. 2010 and citations therein). It is possible that the impacts for a given model forecast with large uncertainty (e.g., like the convection along the dryline for the event studied here) could be improved if quantitative methods are used to guide the times and locations of the sampling. Efforts are under way to determine the feasibility of this approach using an EnKF method and ensemble sensitivity analysis approach (e.g., Bednarczyk and Ancell 2015) to maximize the positive impact of assimilating soundings on forecasts of convective storms.

Finally, this study deliberately did not assimilate radar or satellite data into the initial model condition so that the impacts of the sounding assimilation could be isolated effectively. Assimilation of clear-air radial velocity observations from radar data and retrievals of temperature and water vapor from satellite radiances (e.g., Jones et al. 2015) may improve the mesoscale background environment further. As storms develop, radar data should be assimilated to introduce the existing storms, and their effects on the environment, into the model initial conditions (e.g., Dowell et al. 2011; Snook et al. 2012; Wheatley et al. 2014), as well as suppress spurious storm development in model forecasts. However, in order for radar data assimilation to be effective, key meteorological features that support the convection (e.g., fronts, drylines) need to be represented accurately in the mesoscale background (Aksoy et al. 2009; Stensrud and Gao 2010; Dong et al. 2011; Yussouf et al. 2015). In the case presented here, the assimilation of the MPEX soundings increased the low-level convergence along a front and the subsequent convection-permitting forecasts had more skill in placing the storms. Furthermore, the low- to midlevel moisture was reduced in an area where the MPEX run correctly reduced the development of spurious storms. Future

Brought to you by NOAA Central Library | Unauthenticated | Downloaded 09/22/21 06:55 PM UTC

studies should examine the potential added benefits of nearby sounding assimilation in concurrent mesoscale/convective-scale assimilation systems (e.g., Yussouf et al. 2015) that include radar data in the cycled assimilation procedure to determine if the sounding assimilation, and its potential to improve the location of fronts, midlevel dry air, etc., in the mesoscale background, augments the positive impacts of radar data assimilation on subsequent forecasts.

Acknowledgments. The authors thank Scott Steiger of SUNY Oswego for providing their sounding data. Helpful comments and suggestions were provided by Glen Romine, Dusty Wheatley, Adam Clark, and two anonymous reviewers. A number of people in the University of Oklahoma School of Meteorology community and the Colorado State Atmospheric science department provided support, feedback, and valuable discussion; thanks in particular to the following: committee members Alan Shapiro and Xuguang Wang, Dave Parsons, Nicholas Szapiro, Russ Schumacher, Greg Herman, and Erik Nielsen. We thank the Field Observing Facilities Support team at NSSL, particularly Sean Waugh, for constructing the mobile sounding systems for MPEX. A portion of the computing for this project was performed at the OU Supercomputing Center for Education and Research (OSCER) at the University of Oklahoma (OU). This project was supported by funding from the NOAA/Office of Oceanic and Atmospheric Research under NOAA–University of Oklahoma Cooperative Agreement NA11OAR4320072, the U.S. Department of Commerce, and by the National Science Foundation Award 1230114.

REFERENCES

Aksoy, A., D. C. Dowell, and C. Snyder, 2009: A multicase comparative assessment of the ensemble Kalman filter for assimilation of radar observations. Part I: Storm-scale analyses. *Mon. Wea. Rev.*, **137**, 1805–1824, doi:10.1175/2008MWR2691.1.

Ancell, B. C., 2012: Examination of analysis and forecast errors of high-resolution assimilation, bias removal, and digital filter initialization with an ensemble Kalman filter. *Mon. Wea. Rev.*, **140**, 3992–4004, doi:10.1175/MWR-D-11-00319.1.

Anderson, J. L., 2001: An ensemble adjustment Kalman filter for data assimilation. *Mon. Wea. Rev.*, **129**, 2884–2903, doi:10.1175/1520-0493(2001)129<2884:AEAKFF>2.0.CO;2.

——, 2007: An adaptive covariance inflation error correction algorithm for ensemble filters. *Tellus*, **59**, 210–224, doi:10.1111/j.1600-0870.2006.00216.x.

——, and N. Collins, 2007: Scalable implementations of ensemble filter algorithms for data assimilation. *J. Atmos. Oceanic Technol.*, **24**, 1452–1463, doi:10.1175/JTECH2049.1.

——, T. Hoar, K. Raeder, H. Liu, N. Collins, R. Torn, and A. Avellano, 2009: The Data Assimilation Research Testbed: A community facility. *Bull. Amer. Meteor. Soc.*, **90**, 1283–1296, doi:10.1175/2009BAMS2618.1.

Bedka, K. M., C. S. Velden, R. A. Petersen, W. F. Feltz, and J. R. Mecikalski, 2009: Comparisons of satellite-derived atmospheric motion vectors, rawinsondes, and NOAA wind profiler observations. *J. Appl. Meteor. Climatol.*, **48**, 1542–1561, doi:10.1175/2009JAMC1867.1.

Bednarczyk, C. N., and B. C. Ancell, 2015: Ensemble sensitivity analysis applied to a southern plains convective event. *Mon. Wea. Rev.*, **143**, 230–249, doi:10.1175/MWR-D-13-00321.1.

Benjamin, S. G., B. D. Jamison, W. R. Moninger, S. R. Sahm, B. E. Schwartz, and T. W. Schlatter, 2010: Relative short-range forecast impact from aircraft, profiler, radiosonde, VAD, GPS-PW, METAR, and mesonet observations via the RUC hourly assimilation cycle. *Mon. Wea. Rev.*, **138**, 1319–1343, doi:10.1175/2009MWR3097.1.

Cintineo, R. M., and D. J. Stensrud, 2013: On the predictability of supercell thunderstorm evolution. *J. Atmos. Sci.*, **70**, 1993–2011, doi:10.1175/JAS-D-12-0166.1.

Clark, A. J., and Coauthors, 2012: An overview of the 2010 Hazardous Weather Testbed experimental forecast program spring experiment. *Bull. Amer. Meteor. Soc.*, **93**, 55–74, doi:10.1175/BAMS-D-11-00040.1.

Coniglio, M. C., 2012: Verification of RUC 0-1-h forecasts and SPC mesoscale analyses using VORTEX2 soundings. *Wea. Forecasting*, **27**, 667–683, doi:10.1175/WAF-D-11-00096.1.

Dawson, D. T., II, L. J. Wicker, E. R. Mansell, and R. L. Tanamachi, 2012: Impact of the environmental low-level wind profile on ensemble forecasts of the 4 May 2007 Greensburg, Kansas, tornadic storm and associated mesocyclones. *Mon. Wea. Rev.*, **140**, 696–716, doi:10.1175/MWR-D-11-00008.1.

Dong, J., M. Xue, and K. Droegemeier, 2011: The analysis and impact of simulated high-resolution surface observations in addition to radar data for convective storms with an ensemble Kalman filter. *Meteor. Atmos. Phys.*, **112**, 41–61, doi:10.1007/s00703-011-0130-3.

Dowell, D. C., F. Zhang, L. J. Wicker, C. Snyder, and N. A. Crook, 2004: Wind and temperature retrievals in the 17 May 1981 Arcadia, Oklahoma, supercell: Ensemble Kalman filter experiments. *Mon. Wea. Rev.*, **132**, 1982–2005, doi:10.1175/1520-0493(2004)132<1982:WATRIT>2.0.CO;2.

——, L. J. Wicker, and C. Snyder, 2011: Ensemble Kalman filter assimilation of radar observations of the 8 May 2003 Oklahoma City supercell: Influences of reflectivity observations on storm-scale analyses. *Mon. Wea. Rev.*, **139**, 272–294, doi:10.1175/2010MWR3438.1.

Evensen, G., 1994: Sequential data assimilation with a nonlinear quasi-geostrophic model using Monte Carlo methods to forecast error statistics. *J. Geophys. Res.*, **99**, 10 143–10 162, doi:10.1029/94JC00572.

Fabry, F., 2010: For how long should what data be assimilated for the mesoscale forecasting of convection and why? Part II: On the observation signal from different sensors. *Mon. Wea. Rev.*, **138**, 256–264, doi:10.1175/2009MWR2884.1.

——, and J. Sun, 2010: For how long should what data be assimilated for the mesoscale forecasting of convection and why? Part I: On the propagation of initial condition errors and their implications for data assimilation. *Mon. Wea. Rev.*, **138**, 242–255, doi:10.1175/2009MWR2883.1.

Fujita, T., D. J. Stensrud, and D. C. Dowell, 2007: Surface data assimilation using an ensemble Kalman filter approach with initial condition and model physics uncertainties. *Mon. Wea. Rev.*, **135**, 1846–1868, doi:10.1175/MWR3391.1.

Gaspari, G., and S. E. Cohn, 1999: Construction of correlation functions in two and three dimensions. *Quart. J. Roy. Meteor. Soc.*, **125**, 723–757, doi:10.1002/qj.49712555417.

Brought to you by NOAA Central Library | Unauthenticated | Downloaded 09/22/21 06:55 PM UTC

Gelaro, R., R. H. Langland, S. Pellerin, and R. Todling, 2010: The THORPEX observation impact intercomparison experiment. *Mon. Wea. Rev.*, **138**, 4009–4025, doi:10.1175/2010MWR3393.1.

Hakim, G. J., and R. D. Torn, 2008: Ensemble synoptic analysis. *Synoptic–Dynamic Meteorology and Weather Analysis and Forecasting: A Tribute to Fred Sanders*, L. F. Bosart and H. B. Bluestein, Eds., Amer. Meteor. Soc., 147–161.

Hamill, T. M., 1999: Hypothesis tests for evaluating numerical precipitation forecasts. *Wea. Forecasting*, **14**, 155–167, doi:10.1175/1520-0434(1999)014<0155:HTFENP>2.0.CO;2.

Hane, C. E., C. L. Ziegler, and H. B. Bluestein, 1993: Investigation of the dryline and convective storms initiated along the dryline: Field experiments during COPS-91. *Bull. Amer. Meteor. Soc.*, **74**, 2133–2145, doi:10.1175/1520-0477(1993)074<2133:IOTDAC>2.0.CO;2.

Jewett, B. F., and R. B. Wilhelmson, 2006: The role of forcing in cell morphology and evolution within midlatitude squall lines. *Mon. Wea. Rev.*, **134**, 3714–3734, doi:10.1175/MWR3164.1.

Jones, T. A., J. A. Otkin, D. J. Stensrud, and K. Knopfmeier, 2013: Assimilation of satellite infrared radiances and Doppler radar observations during a cool season observing system simulation experiment. *Mon. Wea. Rev.*, **141**, 3273–3299, doi:10.1175/MWR-D-12-00267.1.

——, D. Stensrud, L. Wicker, P. Minnis, and R. Palikonda, 2015: Simultaneous radar and satellite data storm-scale assimilation using an ensemble Kalman filter approach for 24 May 2011. *Mon. Wea. Rev.*, **143**, 165–194, doi:10.1175/MWR-D-14-00180.1.

Kain, J. S., S. J. Weiss, J. J. Levit, M. E. Baldwin, and D. R. Bright, 2006: Examination of convection-allowing configurations of the WRF model for the prediction of severe convective weather: The SPC/NSSL spring program 2004. *Wea. Forecasting*, **21**, 167–181, doi:10.1175/WAF906.1.

——, S. R. Dembek, S. J. Weiss, J. L. Case, J. J. Levit, and R. A. Sobash, 2010: Extracting unique information from high-resolution forecast models: Monitoring selected fields and phenomena every time step. *Wea. Forecasting*, **25**, 1536–1542, doi:10.1175/2010WAF2222430.1.

Kalnay, E., 2003: *Atmospheric Modeling, Data Assimilation, and Predictability*. Cambridge University Press, 368 pp.

Knopfmeier, K. H., and D. J. Stensrud, 2013: Influence of mesonet observations on the accuracy of surface analyses generated by an ensemble Kalman filter. *Wea. Forecasting*, **28**, 815–841, doi:10.1175/WAF-D-12-00078.1.

Langland, R., and Coauthors, 1999: The North Pacific Experiment (NORPEX-98): Targeted observations for improved North American weather forecasts. *Bull. Amer. Meteor. Soc.*, **80**, 1363–1384, doi:10.1175/1520-0477(1999)080<1363:TNPENT>2.0.CO;2.

Laroche, S., and R. Sarrazin, 2013: Impact of radiosonde balloon drift on numerical weather prediction and verification. *Wea. Forecasting*, **28**, 772–782, doi:10.1175/WAF-D-12-00114.1.

Li, J., C.-Y. Liu, P. Zhang, and T. J. Schmit, 2012: Applications of full spatial resolution space-based advanced infrared soundings in the preconvection environment. *Wea. Forecasting*, **27**, 515–524, doi:10.1175/WAF-D-10-05057.1.

Liu, Z.-Q., and F. Rabier, 2002: The interaction between model resolution, observation resolution and observation density in data assimilation: A one-dimensional study. *Quart. J. Roy. Meteor. Soc.*, **128**, 1367–1386, doi:10.1256/003590002320373337.

Marquis, J., Y. Richardson, P. Markowski, D. Dowell, J. Wurman, K. Kosiba, P. Robinson, and G. Romine, 2014: An investigation of the Goshen County, Wyoming, tornadic supercell of 5 June 2009 using EnKF assimilation of mobile mesonet and radar observations collected during VORTEX2. Part I: Experiment design and verification of the EnKF analyses. *Mon. Wea. Rev.*, **142**, 530–554, doi:10.1175/MWR-D-13-00007.1.

Miller, P. A., M. Barth, L. Benjamin, R. Artz, and W. Pendergrass, 2007: MADIS support for UrbaNet. *14th Symp. on Meteorological Observations, and Instrumentation*, San Antonio, TX, Amer. Meteor. Soc., JP2.5. [Available online at https://ams.confex.com/ams/87ANNUAL/techprogram/paper_119116.htm.]

Murphy, A. H., and E. S. Epstein, 1989: Skill scores and correlation coefficients in model verification. *Mon. Wea. Rev.*, **117**, 572–582, doi:10.1175/1520-0493(1989)117<0572:SSACCI>2.0.CO;2.

Roberts, N. M., and H. W. Lean, 2008: Scale-selective verification of rainfall accumulations from high-resolution forecasts of convective events. *Mon. Wea. Rev.*, **136**, 78–97, doi:10.1175/2007MWR2123.1.

Romine, G. S., C. S. Schwartz, C. Snyder, J. L. Anderson, and M. L. Weisman, 2013: Model bias in a continuously cycled assimilation system and its influence on convection-permitting forecasts. *Mon. Wea. Rev.*, **141**, 1263–1284, doi:10.1175/MWR-D-12-00112.1.

Schwartz, C. S., and Coauthors, 2010: Toward improved convection-allowing ensembles: Model physics sensitivities and optimizing probabilistic guidance with small ensemble membership. *Wea. Forecasting*, **25**, 263–280, doi:10.1175/2009WAF2222267.1.

Snook, N., M. Xue, and Y. Jung, 2011: Analysis of a tornadic mesoscale convective vortex based on ensemble Kalman filter assimilation of CASA X-band and WSR-88D radar data. *Mon. Wea. Rev.*, **139**, 3446–3468, doi:10.1175/MWR-D-10-05053.1.

——, ——, and ——, 2012: Ensemble probabilistic forecasts of a tornadic mesoscale convective system from ensemble Kalman filter analyses using WSR-88D and CASA radar data. *Mon. Wea. Rev.*, **140**, 2126–2146, doi:10.1175/MWR-D-11-00117.1.

Snyder, C., and F. Zhang, 2003: Assimilation of simulated Doppler radar observations with an ensemble Kalman filter. *Mon. Wea. Rev.*, **131**, 1663–1677, doi:10.1175//2555.1.

Sobash, R. A., and D. J. Stensrud, 2015: Assimilating surface mesonet observations with the EnKF to improve ensemble forecasts of convection initiation on 29 May 2012. *Mon. Wea. Rev.*, **143**, 3700–3725, doi:10.1175/MWR-D-14-00126.1.

Stensrud, D. J., and J. Gao, 2010: Importance of horizontally inhomogeneous environmental initial conditions to ensemble storm-scale radar data assimilation and very short-range forecasts. *Mon. Wea. Rev.*, **138**, 1250–1272, doi:10.1175/2009MWR3027.1.

——, and Coauthors, 2009: Convective-scale warn-on-forecast system: A vision for 2020. *Bull. Amer. Meteor. Soc.*, **90**, 1487–1499, doi:10.1175/2009BAMS2795.1.

Stratman, D. R., M. C. Coniglio, S. E. Koch, and M. Xue, 2013: Use of multiple verification methods to evaluate forecasts of convection from hot-and cold-start convection-allowing models. *Wea. Forecasting*, **28**, 119–138, doi:10.1175/WAF-D-12-00022.1.

Talagrand, O., 1997: Assimilation of observations, an introduction. *J. Meteor. Soc. Japan*, **75**, 81–99.

Torn, R. D., and G. J. Hakim, 2008: Ensemble-based sensitivity analysis. *Mon. Wea. Rev.*, **136**, 663–677, doi:10.1175/2007MWR2132.1.

Trapp, R. J., D. J. Stensrud, M. C. Coniglio, R. S. Schumacher, M. E. Baldwin, S. Waugh, and D. T. Conlee, 2016: Mobile radiosonde deployments during the Mesoscale Predictability Experiment (MPEX): Rapid and adaptive sampling of upscale

Brought to you by NOAA Central Library | Unauthenticated | Downloaded 09/22/21 06:55 PM UTC

convective feedbacks. *Bull. Amer. Meteor. Soc.*, **97**, 329–336, doi:10.1175/BAMS-D-14-00258.1.

Wandishin, M. S., D. J. Stensrud, S. L. Mullen, and L. J. Wicker, 2010: On the predictability of mesoscale convective systems: Three-dimensional simulations. *Mon. Wea. Rev.*, **138**, 863–885, doi:10.1175/2009MWR2961.1.

Weaver, J. F., and S. P. Nelson, 1982: Multiscale aspects of thunderstorm gust fronts and their effects on subsequent storm development. *Mon. Wea. Rev.*, **110**, 707–718, doi:10.1175/1520-0493(1982)110<0707:MAOTGF>2.0.CO;2.

Weisman, M. L., C. Davis, W. Wang, K. W. Manning, and J. B. Klemp, 2008: Experiences with 036-h explicit convective forecasts with the WRF-ARW Model. *Wea. Forecasting*, **23**, 407–437, doi:10.1175/2007WAF2007005.1.

——, and Coauthors, 2015: The Mesoscale Predictability Experiment (MPEX). *Bull. Amer. Meteor. Soc.*, **96**, 2127–2149, doi:10.1175/BAMS-D-13-00281.1.

Weygandt, S. S., A. F. Loughe, S. G. Benjamin, and J. L. Mahoney, 2004: Scale sensitivities in model precipitation skill scores during IHOP. *22nd Conf. on Severe Local Storms*, Hyannis, MA, Amer. Meteor. Soc., 16A.8. [Available online at https://ams.confex.com/ams/11aram22sls/techprogram/paper_81986.htm.]

Wheatley, D. M., D. J. Stensrud, D. C. Dowell, and N. Yussouf, 2012: Application of a WRF mesoscale data assimilation system to springtime severe weather events 2007–09. *Mon. Wea. Rev.*, **140**, 1539–1557, doi:10.1175/MWR-D-11-00106.1.

——, N. Yussouf, and D. J. Stensrud, 2014: Ensemble Kalman filter analyses and forecasts of a severe mesoscale convective system using different choices of microphysics schemes. *Mon. Wea. Rev.*, **142**, 3243–3263, doi:10.1175/MWR-D-13-00260.1.

——, K. H. Knopfmeier, T. A. Jones, and G. J. Creager, 2015: Storm-scale data assimilation and ensemble forecasting with the NSSL experimental warn-on-forecast system. Part I: Radar data experiments. *Wea. Forecasting*, **30**, 1795–1817, doi:10.1175/WAF-D-15-0043.1.

Wulfmeyer, V., and Coauthors, 2015: A review of the remote sensing of lower tropospheric thermodynamic profiles and its indispensable role for the understanding and the simulation of water and energy cycles. *Rev. Geophys.*, **53**, 819–895, doi:10.1002/2014RG000476.

Wurman, J., K. Kosiba, P. Robinson, and T. Marshall, 2014: The role of multiple-vortex tornado structure in causing storm researcher fatalities. *Bull. Amer. Meteor. Soc.*, **95**, 31–45, doi:10.1175/BAMS-D-13-00221.1.

Yussouf, N., D. C. Dowell, L. J. Wicker, K. H. Knopfmeier, and D. M. Wheatley, 2015: Storm-scale data assimilation and ensemble forecasts for the 27 April 2011 severe weather outbreak in Alabama. *Mon. Wea. Rev.*, **143**, 3044–3066, doi:10.1175/MWR-D-14-00268.1.

Zhang, F., Z. Meng, and A. Aksoy, 2006: Tests of an ensemble Kalman filter for mesoscale and regional-scale data assimilation. Part I: Perfect model experiments. *Mon. Wea. Rev.*, **134**, 722–736, doi:10.1175/MWR3101.1.

——, N. Bei, R. Rotunno, C. Snyder, and C. C. Epifanio, 2007: Mesoscale predictability of moist baroclinic waves: Convection-permitting experiments and multistage error growth dynamics. *J. Atmos. Sci.*, **64**, 3579–3594, doi:10.1175/JAS4028.1.

Zhang, J., and Coauthors, 2011: National Mosaic and Multi-sensor QPE (NMQ) system: Description, results, and future plans. *Bull. Amer. Meteor. Soc.*, **92**, 1321–1338, doi:10.1175/2011BAMS-D-11-00047.1.

Brought to you by NOAA Central Library | Unauthenticated | Downloaded 09/22/21 06:55 PM UTC